RSC Advances

PAPER

View Article Online
View Journal | View Issue

Cite this: *RSC Adv.*, 2026, **16**, 25144

A QbD-optimized magnetic MOF-chitosan nanocarrier for targeted curcumin delivery and synergistic antimicrobial activity

Donia Hemida,[a] Nabila Shehata,[b] Nada Elgiddawy,[a] Haifa E. Alfassam,[c] Samar M. Mahgoub[d] and Rehab Mahmoud *[ef]

Antimicrobial resistance and cancer represent critical global health challenges that demand smarter, targeted drug delivery strategies. This study reports the systematic design, Quality by Design (QbD)-driven optimization, and comprehensive characterization of curcumin-loaded magnetic metal–organic framework–chitosan nanocomposites (Cur/Fe_3O_4@ZIF-8@CS) as a multifunctional nanoplatform integrating pH-responsive drug release, magnetic targeting, and broad-spectrum antimicrobial activity. A Box–Behnken experimental design was employed to optimize three critical formulation variables including MOF-to-drug ratio (X_1), chitosan concentration (X_2), and iron oxide content (X_3) against four predefined Critical Quality Attributes (CQAs): particle size, zeta potential, PDI, and encapsulation efficiency. The optimized nanocomposite achieved a particle size of 228.6 ± 4.7 nm, a zeta potential of +31.5 mV, a PDI of 0.218, and an encapsulation efficiency of 87.4 ± 2.3%. Successful step-by-step assembly was confirmed by DLS, ATR-FTIR of all individual components and the final composite, TEM with size-distribution mapping, and VSM magnetometry. Drug release was sustained and pH-dependent, reaching 63.8% at pH 5.5 *versus* 58.4% at pH 7.4 after 72 hours, following anomalous non-Fickian transport kinetics (Korsmeyer–Peppas $n = 0.61$). The nanocomposite exhibited potent antimicrobial activity with MIC values up to 66-fold lower than free curcumin against *Escherichia coli*, and 2.5- to 45-fold lower across the remaining tested organisms. A two-month physicochemical stability study conducted under long-term (25 ± 2 °C) and accelerated (40 ± 2 °C/75 ± 5% RH, ICH Q1A(R2)) conditions confirmed that all critical quality attributes remained within acceptable pharmaceutical limits, with curcumin retention of 94.6 ± 1.8% at 25 °C and 87.9 ± 2.6% at 40 °C after two months. Cytotoxicity assessment by MTT assay on L929 mouse fibroblast cells yielded IC_{50} values of 206.65 μg mL^{-1} for the blank nanocomposite (Fe_3O_4@ZIF-8@CS) and 273.15 μg mL^{-1} for the curcumin-loaded formulation (Cur/Fe_3O_4@ZIF-8@CS), confirming acceptable biocompatibility at therapeutically relevant concentrations. These findings collectively establish Cur/Fe_3O_4@ZIF-8@CS as a rationally designed, multifunctional nanoplatform with significant potential for combined antimicrobial and anticancer targeted therapy.

Received 23rd March 2026
Accepted 16th April 2026

DOI: 10.1039/d6ra02404a

rsc.li/rsc-advances

1 Introduction

Antimicrobial resistance (AMR) and cancer are two of the most serious health problems in the world today.[1] The World Health Organization reported that resistant bacterial infections caused about 1.27 million deaths in 2019, and this number is expected to rise sharply in the coming decades.[2,3] At the same time, cancer causes close to 10 million deaths each year globally. Both diseases share a common challenge: many existing drugs either do not work well enough, cause harmful side effects, or lose their effectiveness over time because bacteria or cancer cells evolve to evade them.[4] These problems have prompted researchers to seek smarter, more targeted methods for drug delivery.

Nanotechnology offers a promising solution. By carrying drugs inside very small particles, scientists can protect the drug

[a]*Department of Biotechnology and Life Sciences, Faculty of Postgraduate Studies for Advanced Sciences (PSAS), Beni-Suef University, Beni-Suef, 62511, Egypt. E-mail: doniahazem55@gmail.com; N.giddawy@psas.bsu.edu.eg*

[b]*Environmental Science and Industrial Development Department, Faculty of Postgraduate Studies for Advanced Sciences, Beni-Suef University, Beni-Suef, Egypt. E-mail: nabila.shehata@psas.bsu.edu.eg*

[c]*Department of Biology, College of Science, Princess Nourah bint Abdulrahman University, P. O. BOX 84428, Riyadh 11671, Saudi Arabia*

[d]*Materials Science and Nanotechnology Department, Faculty of Postgraduate Studies for Advanced Sciences, Beni-Suef University, Egypt. E-mail: Miramar15@yahoo.com*

[e]*Chemistry Department, Faculty of Science, Beni-Suef University, Beni-Suef 62511, Egypt. E-mail: rehabkhaled@science.bsu.edu.eg*

[f]*Department of Chemistry, Faculty of Science, Chulalongkorn University, Bangkok 10330, Thailand*

from breaking down too early, deliver it more precisely to the diseased site, and release it gradually so that it keeps working for longer.[5–7] One particularly interesting type of nanocarrier is the metal–organic framework (MOF). MOFs are tiny porous crystals built from metal ions connected by organic linkers, forming a highly ordered structure full of small channels and pores.[8] This large internal surface area allows MOFs to hold a high amount of drug inside them. One well-studied MOF is ZIF-8, which is made from zinc ions and 2-methylimidazole. ZIF-8 has an important feature: it starts to break apart at acidic pH, which means it can release its drug cargo preferentially in acidic environments like tumors or infected tissue.[9–12]

Iron oxide magnetic nanoparticles (Fe_3O_4), also called SPIONs, are another useful component. These particles respond to external magnetic fields, which makes it possible to guide them to a specific site in the body. They also do not retain any magnetism once the magnetic field is removed, so they do not clump together in the bloodstream.[13,14] When iron oxide particles are combined with MOFs, the resulting hybrid carrier can both hold a large amount of drug and be steered to the target site.[15]

Chitosan is a natural sugar-based polymer made from the shells of shrimp and other crustaceans. It is safe, biodegradable, and sticks well to biological surfaces. Its positive charge at acidic pH allows it to disrupt bacterial cell membranes and helps the nanoparticle bind to cells.[16] Coating a nanoparticle with chitosan, therefore adds its own antibacterial activity on top of whatever drug is being delivered.[17–19]

Curcumin is the yellow pigment found in turmeric. It has been widely studied for its ability to fight bacteria, reduce inflammation, and slow the growth of cancer cells.[20] However, curcumin has one major practical problem: it is almost completely insoluble in water, and when taken orally, very little of it actually reaches the bloodstream. It also breaks down quickly in the body. These limitations have prevented curcumin from being used as a standalone medicine despite its strong biological activity.[21] Loading curcumin into a nanocarrier system can protect it from degradation, increase how much of it reaches the target tissue, and control how it is released.[22–24]

Combining all three components, ZIF-8 MOF, Fe_3O_4 magnetic nanoparticles, and chitosan into a single system creates a nanocarrier that works on multiple levels at once: high drug loading from the MOF, magnetic targeting from the iron oxide, pH-responsive release from the ZIF-8 degradation, and additional antibacterial action from the chitosan coating.

To develop this system in a scientific and efficient way, we used a Quality by Design (QbD) approach based on the Box–Behnken experimental design. QbD is a method recommended by international pharmaceutical guidelines (ICH Q8) that replaces trial-and-error testing with a structured plan to understand how formulation variables affect product quality.[25,26] The Box–Behnken design allowed us to test multiple formulation conditions at the same time and find the best combination using mathematical models, rather than testing every possible combination one by one.[27]

This study therefore aimed to: (1) prepare curcumin-loaded magnetic MOF–chitosan nanocomposites (Cur/Fe_3O_4@ZIF-8@CS); (2) optimize the formulation using a Box–Behnken QbD design with four quality responses including particle size, zeta potential, PDI, and encapsulation efficiency; (3) characterize the product step by step using DLS, TEM, and magnetic measurements; (4) compare drug release from the nanocomposite against free curcumin at two different pH values; and (5) test the antibacterial and antifungal activity of the final product; and (6) evaluate the physicochemical stability of the optimized nanocomposite under long-term (25 ± 2 °C) and accelerated (40 ± 2 °C/75 ± 5% RH, ICH Q1A(R2)) storage conditions over two months, tracking particle size, PDI, zeta potential, and curcumin content retention as critical quality attributes; and (7) assess the *in vitro* cytotoxicity of both the blank and curcumin-loaded nanocomposites on L929 mouse fibroblast cells using the MTT assay. The cytotoxicity study revealed IC_{50} values of 206.65 μg mL^{-1} (Fe_3O_4@ZIF-8@CS) and 273.15 μg mL^{-1} (Cur/Fe_3O_4@ZIF-8@CS) against L929 fibroblasts, with the curcumin-loaded formulation showing a higher IC_{50} and thus lower cytotoxicity to normal cells, supporting its safety profile at therapeutic concentrations.

2 Materials and methods

2.1 Materials

Curcumin (≥98% purity, HPLC grade), zinc nitrate hexahydrate, 2-methylimidazole, ferric chloride hexahydrate, ferrous chloride tetrahydrate, ammonia solution (28%), and low-molecular-weight chitosan (190 kDa) were purchased from Sigma-Aldrich (St. Louis, MO, USA). Glacial acetic acid, dimethyl sulfoxide (DMSO), methanol, and ethanol were from Merck KGaA (Darmstadt, Germany). Tryptone Soya Broth (TSB, Oxoid, cat. no. CM0129B), Brain Heart Infusion Agar (BHI Agar, Oxoid, cat. no. CM1136B), and Sabouraud dextrose broth (Oxoid) were from Oxoid Ltd (Basingstoke, UK). All water used in experiments was ultrapure (≥18.2 MΩ cm, Milli-Q system). Phosphate-buffered saline (PBS, pH 7.4) and acetate buffer (pH 5.5) were freshly prepared as described in Section 2.5.

2.2 Box–Behnken experimental design

Before starting the experiments, we defined four target quality criteria for the final nanocomposite, called Critical Quality Attributes (CQAs): particle size between 150 and 300 nm (small enough to accumulate in tumors through the EPR effect), zeta potential above +20 mV (to keep particles stable in suspension and help them bind to bacterial cells), PDI below 0.30 (to ensure the particles are uniform in size), and encapsulation efficiency above 80% (to ensure enough drug is loaded into each particle). These targets were based on established requirements for therapeutic nanoparticles and were set before any experiments were run.[28]

We then identified three formulation variables (independent factors) that were most likely to affect these quality targets, based on a risk assessment: the ratio of MOF to drug (X_1), the chitosan concentration used for coating (X_2), and the iron oxide content of the composite (X_3). Each factor was tested at three levels: low (−1), medium (0), and high (+1), as shown in Table 1.

Table 1 Independent formulation factors and their tested levels in the Box–Behnken design

Factor	Symbol	Low (−1)	Center (0)	High (+1)
MOF-to-drug ratio (w/w)	X_1	1 : 1	2 : 1	3 : 1
Chitosan concentration (mg mL^{-1})	X_2	1.0	2.0	3.0
Fe_3O_4 content (% w/w)	X_3	5	10	15

The Box–Behnken design produced 17 formulations: 12 formulations that test combinations of factor extremes, and 5 repeated formulations at the central (mid-level) conditions to estimate experimental error. All 17 formulations were prepared on different days in a random order to avoid any bias from day-to-day changes. For each formulation, we measured all four CQAs: particle size (Y_1, nm), zeta potential (Y_2, mV), PDI (Y_3), and encapsulation efficiency (Y_4, %).

Encapsulation efficiency was measured by UV-vis spectrophotometry (Shimadzu UV-2600, Japan) at 425 nm. After preparing each formulation and collecting it by centrifugation, the amount of curcumin that wasn't encapsulated (remaining in the washing solutions) was measured and subtracted from the total amount added. A calibration curve was made in DMSO: water (1 : 1, v/v) over a range of 0.5–25 μg mL^{-1} ($R^2 = 0.9997$). EE% and drug loading (DL%) were calculated as:

$$\text{EE (\%)} = [(\text{total curcumin added} - \text{free curcumin})/\text{total curcumin added}] \times 100 \quad (1)$$

$$\text{DL (\%)} = [(\text{total curcumin added} - \text{free curcumin})/\text{total nanocomposite mass}] \times 100 \quad (2)$$

Each response was fitted to a second-order polynomial equation using Minitab® v21.0:

$$Y = \beta_0 + \beta_1 X_1 + \beta_2 X_2 + \beta_3 X_3 + \beta_{12} X_1 X_2 + \beta_{13} X_1 X_3 + \beta_{23} X_2 X_3 + \beta_{11} {X_1}^2 + \beta_{22} {X_2}^2 + \beta_{33} {X_3}^2 \quad (3)$$

where Y is the predicted response value and the β terms are the regression coefficients. Model quality was checked using ANOVA, R^2, adjusted R^2, predicted R^2, and adequate precision (a signal-to-noise ratio; values above 4 are acceptable). The best formulation was found by running a numerical desirability function optimization that simultaneously minimized particle size (goal: minimize; lower limit 150 nm, upper limit 300 nm) and PDI (goal: minimize; upper limit 0.30) while maximizing zeta potential (goal: maximize; lower limit +20 mV) and encapsulation efficiency (goal: maximize; lower limit 80%), each with equal weighting. The composite desirability score (D, ranging from 0 to 1) was used to rank and select the optimum formulation.[29]

Three-dimensional (3D) response surface plots and the corresponding two-dimensional (2D) contour plots were generated directly from each fitted quadratic model using Minitab® v21.0. For each of the four CQAs, three pairs of plots were produced by varying two factors simultaneously across their experimental range while fixing the third factor at its center-point level: (i) X_1 *vs.* X_2 at $X_3 = 0$ (10% w/w Fe_3O_4); (ii) X_1 *vs.* X_3 at $X_2 = 0$ (2.0 mg per mL chitosan); and (iii) X_2 *vs.* X_3 at $X_1 = 0$ (2 : 1 MOF-to-drug ratio). The 3D surface plots illustrate the overall curvature and magnitude of the response across the design space, whereas the overlaid 2D contour maps delineate iso-response contours that facilitate identification of factor combinations satisfying multiple quality targets simultaneously. The Box–Behnken design was selected in preference to a full factorial or central composite design because it requires only three levels per factor, avoids simultaneous extreme-level combinations (corner points) that may be physically unrealizable or excessively resource-intensive, and achieves a near-rotatable geometry with a substantially smaller number of runs.[29]

2.3 Preparation of nanocomposites

2.3.1 Step 1: preparation of Fe_3O_4 magnetic nanoparticles. Iron oxide nanoparticles were made by a co-precipitation method. Solutions of $FeCl_3 \cdot 6H_2O$ (2.70 g) and $FeCl_2 \cdot 4H_2O$ (0.99 g) were dissolved separately in deionized water and mixed together under nitrogen gas to prevent oxidation. The mixture was heated to 80 °C with stirring, then 25 mL of ammonia solution was added slowly to trigger particle formation. After 30 minutes, the black magnetic particles were collected using a permanent magnet, washed with water and ethanol to remove impurities, and stored in deionized water (10 mg mL^{-1}) at 4 °C.[30]

2.3.2 Step 2: loading curcumin into the MOF shell (Fe_3O_4@ZIF-8/Cur). Curcumin was trapped inside the ZIF-8 framework during its formation in a one-pot process that avoids extra loading steps. Methanol was selected as the dispersion medium for this step because curcumin is virtually insoluble in water (aqueous solubility ~11 ng mL^{-1} at room temperature) but freely soluble in methanol, enabling homogeneous distribution of curcumin molecules throughout the Fe_3O_4 dispersion prior to ZIF-8 crystallization; direct dispersion in water was therefore not feasible.[20,31,32] For the optimized center-point formulation ($X_1 = 2 : 1$, $X_3 = 10\%$ w/w Fe_3O_4), 10 mg of Fe_3O_4 nanoparticles and 5 mg of curcumin were co-dispersed in 10 mL of methanol and subjected to probe ultrasonication (Q125 Sonicator®, 40% amplitude, 10 min, pulsed 3 s on/1 s off) to produce a uniform, stable dispersion. For all other Box–Behnken design runs, the quantities of Fe_3O_4 and curcumin were scaled proportionally to achieve the MOF-to-drug ratios and Fe_3O_4 content levels defined in Table 1. A 0.4 M 2-methylimidazole solution was prepared by dissolving 3.28 g of 2-methylimidazole in 100 mL of distilled water with stirring at room temperature until a clear, homogeneous solution was obtained. A zinc nitrate hexahydrate solution (0.3 M; prepared by dissolving 89.4 mg of $Zn(NO_3)_2 \cdot 6H_2O$ in 10 mL of distilled water) was then added dropwise to the

Fe_3O_4/curcumin dispersion under continuous magnetic stirring (500 rpm), followed immediately by the 2-methylimidazole solution. This yielded a Zn^{2+} : 2-methylimidazole molar ratio of 1 : 8, consistent with the established stoichiometry for room-temperature ZIF-8 synthesis that ensures complete framework crystallization and high drug encapsulation efficiency.[33,34] The ZIF-8 framework crystallized around the magnetic cores at room temperature over 4 h, enclosing curcumin molecules inside its pores. The resulting Fe_3O_4@ZIF-8/Cur particles were collected by centrifugation (10 000 × *g*, 15 min), washed with methanol three times to remove any unentrapped curcumin, and dispersed in dilute acetic acid (0.1 M) for the next step.[33]

2.3.3 Step 3: chitosan coating (Cur/Fe_3O_4@ZIF-8@CS). Chitosan was dissolved in dilute acetic acid (0.1 M) at the required concentration and filtered. The ZIF-8 particle dispersion was added slowly into the chitosan solution while sonicating, at pH 5.0. At this pH, chitosan carries a strong positive charge (protonated $-NH_3^+$ groups) and adsorbs onto the surface of the ZIF-8/curcumin particles, which, despite carrying a modest positive surface charge at this stage, possess a lower charge density than the chitosan layer, allowing electrostatic and hydrophobic interactions to drive coating deposition and produce the substantially higher zeta potential observed after coating.[35] The mixture was stirred for 2 hours at room temperature. The coated particles were collected by high-speed centrifugation (15 000 × *g*, 20 min, 4 °C) and washed twice with ultrapure water to remove unbound chitosan. The washed pellet was resuspended in ultrapure water, snap-frozen in liquid nitrogen, and lyophilized (freeze-dried) for 48 hours to yield a stable dry powder. The powder was stored at 4 °C in sealed vials protected from light until use.

2.4 Physicochemical characterization methods

Hydrodynamic particle size, PDI, and zeta potential were measured using a Malvern Zetasizer Nano ZS (UK) at 25 °C. Samples were diluted to 0.1 mg mL^{-1} in their respective dispersion medium before measurement. Each sample was measured three times ($n = 3$), and results are reported as mean ± SD. Measurements were taken at each preparation step (bare Fe_3O_4, intermediate core–shell, and final nanocomposite) to track how the particle properties changed during assembly.

The size and shape of the particles were directly visualized by TEM at 200 kV (JEOL JEM-2100F, Japan). Small drops of each sample (0.1 mg mL^{-1}) were placed on carbon-coated copper grids and stained with 2% phosphotungstic acid to make the chitosan layer visible.

The magnetic behavior of Fe_3O_4 MNPs and the final nanocomposite was measured using a vibrating sample magnetometer (VSM, Lakeshore 7400) at room temperature. The saturation magnetization (the maximum magnetic response) was recorded for each sample. Fourier-transform infrared (FTIR) spectroscopy was performed on each individual component and the final nanocomposite to confirm successful integration of all four materials. Samples were analyzed using an ATR-FTIR spectrometer (Bruker Alpha II, Germany) using KBr pellets over the wavenumber range 400–4000 cm^{-1} at a resolution of 4 cm^{-1}, averaging 32 scans per spectrum. Spectra of bare Fe_3O_4 nanoparticles, pure ZIF-8, free low-molecular-weight chitosan, and free curcumin were each recorded individually and then compared with the spectrum of the optimized Cur/Fe_3O_4@ZIF-8@CS nanocomposite powder.

2.5 *In vitro* drug release study

Drug release from the nanocomposite was tested at two pH values: pH 7.4 (PBS, representing normal blood and healthy tissue) and pH 5.5 (acetate buffer, representing the acidic environment inside tumors and infected tissue). Phosphate-buffered saline (PBS, pH 7.4) was prepared by dissolving 8.0 g NaCl, 0.2 g KCl, 1.44 g Na_2HPO_4, and 0.24 g KH_2PO_4 in approximately 900 mL of distilled water, after which the pH was adjusted to 7.4 using 0.1 M HCl or 0.1 M NaOH. The solution volume was then made up to 1000 mL with distilled water and filtered before use. Acetate buffer (pH 5.5) was prepared by dissolving 4.1 g sodium acetate trihydrate ($CH_3COONa \cdot 3H_2O$) in about 900 mL of distilled water, followed by the addition of approximately 2.9 mL glacial acetic acid, and the pH was adjusted to 5.5 using small amounts of acetic acid or NaOH if necessary. The final volume was adjusted to 1000 mL with distilled water, and the solution was filtered before use as the acidic release medium. A parallel experiment using free curcumin dissolved in 0.5% Tween-80 was run under the same conditions as a comparison.

The dialysis bag method was used. A measured amount of nanocomposite (equivalent to 2 mg of curcumin) was placed inside a dialysis membrane bag and placed in 50 mL of release medium at 37 °C with gentle shaking (100 rpm). At set time points from 0.5 h to 72 h, 3 mL samples were taken and replaced with fresh medium to keep sink conditions. Curcumin in each sample was measured by UV absorbance at 425 nm, and the cumulative percent released was calculated.[36]

Drug release at time *t*, cumulative drug release (%) was calculated using eqn (4) and (5):

$$\text{Released drug at time } t = C_t \times V \tag{4}$$

where C_t represents the drug concentration at time *t* (mg mL^{-1}), *V* represents the volume of the dissolution medium (mL).

$$\text{Cumulative drug release (\%)} = \frac{\text{released drug at time } t}{\text{initial amount of drug loaded}} \times 100 \tag{5}$$

2.6 Release kinetics modeling

The release data from both free curcumin and the nanocomposite were fitted to four mathematical models to understand how drug release occurs and to compare the two systems:

Zero-order model eqn (6): drug releases at a constant rate, regardless of how much drug remains.

$$Q_t = Q_0 + K_0 t \tag{6}$$

First-order model eqn (7): the rate of release decreases over time as less drug remains.

$$Q_t = Q_0 e^{(-K_1 t)} \quad (7)$$

Higuchi model eqn (8): drug diffuses out of a solid matrix, following a square root of time relationship.

$$Q_t = K_H t^{0.5} \quad (8)$$

Korsmeyer–Peppas model eqn (9): a flexible model that uses an exponent n to identify the release mechanism. For spherical nanoparticles: $n \leq 0.43$ means simple diffusion (Fickian); $0.43 < n < 0.85$ means both diffusion and polymer swelling contribute (anomalous transport); $n = 0.85$ means swelling fully controls release.

$$M_t/M_\infty = kt^n \quad (9)$$

The best model was chosen based on the highest R^2 and lowest Akaike Information Criterion (AIC) value. All fitting was done using the DDSolver add-in for Microsoft Excel[37] and GraphPad Prism 9.0.

2.7 Antimicrobial activity testing

2.7.1 Microbial strains. The antimicrobial activity of the blank nanocomposite (Fe_3O_4@ZIF-8@CS) and the curcumin-loaded nanocomposite (Cur/Fe_3O_4@ZIF-8@CS) was tested against five clinical microbial strains. These included two Gram-negative bacteria, including *Escherichia coli* (*E. coli*) and *Klebsiella pneumoniae* (*K. pneumoniae*), and two Gram-positive bacteria, including *Staphylococcus aureus* (*S. aureus*) and *Streptococcus agalactiae* (*S. agalactiae*), and one fungal species, *Candida albicans* (*C. albicans*). All strains were obtained from clinical cases and were identified by standard microbiological methods, including culture on selective media and biochemical characterization.

2.7.2 Preparation of microbial suspensions. To prepare working bacterial suspensions, a single colony of each strain was grown in 10 mL of Tryptone Soya Broth (TSB, Oxoid, cat. no. CM0129B) for 18 to 24 h at 37 °C. After incubation, 1.5 mL of the culture was transferred to an Eppendorf tube and centrifuged at 6000 × *g* for 15 minutes at 4 °C. The liquid was discarded, and the microbial cells were washed three times with phosphate-buffered saline (PBS, pH 7.4) to remove any remaining growth medium. Finally, the cells were resuspended in PBS to a concentration matching the 0.5 McFarland turbidity standard, equivalent to approximately 1.5×10^8 colony-forming units per milliliter (CFU mL^{-1}). This standardized concentration was used as the starting inoculum in all antimicrobial tests.

2.7.3 Preparation of test materials. Both test compounds, including the blank nanocomposite (Fe_3O_4@ZIF-8@CS) and the curcumin-loaded nanocomposite (Cur/Fe_3O_4@ZIF-8@CS) were prepared as stock suspensions in 20% dimethyl sulfoxide (DMSO, Oxoid, cat. no. 102952) using magnetic stirring. The suspensions were then homogenized by probe ultrasonication for 5 minutes (Q125 Sonicator®) to ensure even dispersion. The working concentration used in all antimicrobial assays was 1000 μg mL^{-1}.

Free curcumin was additionally included as a third experimental parallel control group in all antimicrobial assays to enable direct, within-experiment quantification of the antibacterial advantage conferred by nanoencapsulation. A stock solution of free curcumin (1000 μg mL^{-1}) was prepared in 0.5% DMSO (v/v in Mueller–Hinton broth for bacterial strains, or Sabouraud dextrose broth for *C. albicans*, as appropriate) with probe ultrasonication (5 min) immediately before use to ensure adequate dispersion. The DMSO vehicle control (0.5% DMSO without curcumin or nanocomposite) was confirmed to produce no inhibition zone in preliminary diffusion assays and was used as a negative vehicle baseline. Curcumin concentration in the stock was verified by UV-vis spectrophotometry at 425 nm against a validated standard curve ($R^2 = 0.9997$) immediately before each assay to confirm solution integrity. This three-arm experimental design (blank nanocomposite/curcumin-loaded nanocomposite/free curcumin) allows rigorous attribution of observed antimicrobial effects to the nanocomposite architecture *versus* the drug alone.

2.7.4 Agar well diffusion assay. The ability of each test compound to inhibit microbial growth was first assessed using the agar well diffusion method. Brain Heart Infusion agar (BHI agar, Oxoid, cat. no. CM1136B) was autoclaved and cooled to 55 °C before being poured into sterile Petri dishes. While still liquid, a bacterial or fungal suspension adjusted to 0.5 McFarland (1.5×10^8 CFU mL^{-1}) was spread evenly onto the agar surface. Once the agar had set, wells of 6 mm diameter were punched through the agar at regular intervals using a sterile cork borer. Each well was filled with 25–30 μL of the test suspension.

Plates were incubated at 37 °C for 24 hours. After incubation, the clear zone of no microbial growth surrounding each well, which is called the zone of inhibition (ZOI), was measured in millimeters using a ruler. A wider zone indicates stronger antimicrobial activity. Positive control wells contained streptomycin (10 μg mL^{-1}) for bacterial strains and fluconazole (25 μg mL^{-1}) for *C. albicans*. All tests were performed in triplicate, and results are reported as mean ± standard deviation (SD).[38]

2.7.5 Minimum inhibitory concentration (MIC) and minimum bactericidal/fungicidal concentration (MBC/MFC). The MIC, which is the lowest concentration of a test compound that completely stops visible microbial growth, was determined by the broth microdilution method according to CLSI guidelines. Starting from a stock concentration of 1000 μg mL^{-1}, each compound was serially diluted two-fold in Mueller–Hinton broth (for bacterial strains) or Sabouraud dextrose broth (for *C. albicans*) in sterile 96-well microtitre plates, producing concentrations ranging from 500 μg mL^{-1} down to 0.0625 μg mL^{-1} in a final volume of 100 μL per well. To each well, 10 μL of the standardized microbial suspension (0.5 McFarland, adjusted to yield a final inoculum of approximately 5×10^5 CFU mL^{-1}) was added. All tubes were incubated at 37 °C for 24 hours. After incubation, tubes were inspected visually for turbidity. The MIC was recorded as the lowest concentration in which no visible cloudiness (turbidity) was observed, indicating complete inhibition of growth.

To determine the MBC (for bacteria) or MFC (for *C. albicans*), a loopful of 50–100 μL from each tube showing no turbidity was streaked onto a drug-free nutrient agar plate. These plates were incubated at 37 °C for 24 hours. The MBC/MFC was defined as the lowest concentration at which no visible colonies grew on the agar, indicating that at least 99.9% of the original inoculum had been killed. All MIC and MBC/MFC tests were performed in triplicate, and results are reported as mean ± SD.

2.7.6 Statistical analysis. All data were analyzed using SPSS software (version 27, IBM Corp., Armonk, NY, USA) and are presented as mean ± SD. A two-way analysis of variance (ANOVA) was applied to examine: (1) the effect of treatment type (blank nanocomposite *vs.* curcumin-loaded nanocomposite), (2) the effect of microbial species, and (3) whether the combination of treatment and organism had any additional effect (interaction). When ANOVA showed a significant main effect, Tukey's post-hoc test was used to find exactly which groups differed from each other. A *p*-value of less than 0.05 was considered statistically significant.

2.8 Cytotoxicity assay

2.8.1 Cell culture. Mouse fibroblast cell line (L929 cells) was provided from the American Type Culture Collection (ATCC, Rockville, MD).

2.8.2 Cell line propagation. Mouse fibroblasts cells were cultured in the supplemented medium (DMEM) with heat inactivated FBS (10.0%), HEPES buffer, gentamycin (50 μg mL^{-1}), and L-glutamine (1.0%) and incubated in 5% CO_2 humidified atmosphere at 37 °C. They were sub cultured 2–3 times per week.

2.8.3 Preparation of stock solution of each tested substance. A stock solution of 100 μg mL^{-1} of the tested formulations (Fe_3O_4@ZIF-8@CS and Cur/Fe_3O_4@ZIF-8@CS) was prepared by reconstitution the 0.1 g in the appropriated volume of 1 mL of DMSO, followed by 5 seconds sonication, aliquotion, and stored at −20 °C until use. The final concentrations of the tested formulation were formulated by diluting the stock with the medium. 0.1% DMSO as a carrier solvent was added to the control cells.

2.8.4 MTT assay. The cells were seeded into a 96-well plate at a density of 1×10^4 cells per well in 100 μL of growth medium. 100 μL of Fe_3O_4@ZIF-8@CS and Cur/Fe_3O_4@ZIF-8@CS was added to the confluent cell monolayers after 24 h of seeding. Control cells were incubated with 0.1% DMSO. Each concentration was tested in triplicate. The plates were kept in CO_2 incubator (5% CO_2) at 37 °C for 24 h, the viability % was assessed using the MTT assay. In which 100 μL of fresh culture DMEM medium without phenol red was replaced the previous culturing medium and 10 μL of a 12 mM MTT stock solution (5 mg of MTT in 1 mL of PBS) was added to each well. Followed by 4 h incubation at the previously mentioned conditions. After that 50 μL of DMSO was replaced 85 μL of the media to dissolve the formazan crystals and the plates incubated for further 10 min. The number of viable cells was determined *via* measuring the optical density (OD) at 590 nm using a microplate reader (TS800, BioTek, Inc, USA) and cell viability was calculated as following:

$$\text{Viability (\%)} = [(OD_t/OD_c)] \times 100\% \quad (10)$$

where OD_t is the mean optical density of wells treated with the test sample and OD_c is the mean optical density of untreated cells.

The relationship between cell survival and drug concentration was plotted to obtain the survival curve for each treatment. IC_{50} was determined from the dose–response curve using GraphPad Prism software (San Diego, CA, USA).[39]

2.9 Stability study

2.9.1 Study design and storage conditions. The physicochemical stability of the optimized Cur/Fe_3O_4@ZIF-8@CS nanocomposite was evaluated under two distinct storage conditions in accordance with ICH Q1A(R2) guidelines:[40] long-term stability at 25 ± 2 °C and accelerated stability at 40 ± 2 °C/75 ± 5% relative humidity (RH). Accelerated testing was conducted in a validated climatic stability chamber (Thermolab Scientific Equipments Pvt. Ltd, Maharashtra, India) equipped with programmable temperature and humidity control units, continuously monitored by a calibrated data logger throughout the study period. Long-term samples were stored at 25 ± 2 °C under controlled laboratory conditions in a temperature-monitored environment, protected from light.

The nanocomposite was accurately weighed into amber borosilicate glass vials (Type I, USP), sealed with polytetrafluoroethylene (PTFE)-lined stoppers and aluminum crimp caps under nitrogen atmosphere to minimize oxidative stress. Vials were stored in an upright orientation. Representative samples were withdrawn in triplicate at three predefined time points: zero time (T_0), one month (T_1), and two months (T_2). At each time point, an independently prepared aliquot was reconstituted in methanol at a concentration of 0.1 mg mL^{-1}, sonicated gently for 30 seconds, and allowed to equilibrate at 25 °C for 10 minutes prior to measurement and measured at 425 nm (Shimadzu UV-2600, Japan) against a validated standard curve (0.5–25 μg mL^{-1}, $R^2 = 0.9997$). Curcumin retention at each time point was calculated as:

$$\text{Curcumin retention (\%)} = (C_t/C_0) \times 100 \quad (11)$$

where C_0 is the curcumin content quantified at T_0 and C_t is the curcumin content at the corresponding sampling time.

2.9.2 Assessed physicochemical parameters. At each time point and for both storage conditions, the following parameters were determined in triplicate ($n = 3$): (i) hydrodynamic particle size (*Z*-average diameter, nm) and polydispersity index (PDI), measured by dynamic light scattering (DLS), and zeta potential (mV) using a Malvern Zetasizer Nano ZS (Malvern Instruments, Worcestershire, UK) at 25 °C, 173° backscatter angle; and (ii) curcumin content retention (%), assessed by UV-vis spectrophotometry.

Physical appearance (color, aggregation, homogeneity upon reconstitution) was assessed visually at each time point.

Table 2 Box–Behnken design matrix and measured responses for all 17 formulations ($n = 3$, mean ± SD). Y_1 = particle size (nm); Y_2 = zeta potential (mV); Y_3 = PDI; Y_4 = encapsulation efficiency (%)

Run	X_1	X_2	X_3	PS (nm) Y_1	ZP (mV) Y_2	PDI Y_3	EE% Y_4
1	−1	−1	0	183 ± 3.2	+22.1 ± 0.9	0.248 ± 0.02	68.2 ± 1.4
2	+1	−1	0	242 ± 4.8	+26.4 ± 1.1	0.276 ± 0.03	74.5 ± 1.8
3	−1	+1	0	196 ± 3.9	+28.7 ± 1.3	0.231 ± 0.02	71.3 ± 1.2
4	+1	+1	0	269 ± 5.3	+32.1 ± 1.4	0.261 ± 0.02	83.6 ± 2.1
5	−1	0	−1	173 ± 2.8	+19.8 ± 0.8	0.239 ± 0.02	66.4 ± 1.6
6	+1	0	−1	252 ± 4.6	+24.5 ± 1.1	0.268 ± 0.02	76.2 ± 1.9
7	−1	0	+1	189 ± 3.4	+21.3 ± 0.9	0.244 ± 0.02	70.1 ± 1.4
8	+1	0	+1	257 ± 5.0	+29.6 ± 1.3	0.272 ± 0.03	80.8 ± 2.2
9	0	−1	−1	178 ± 2.9	+18.7 ± 0.7	0.258 ± 0.02	64.9 ± 1.3
10	0	+1	−1	214 ± 4.1	+27.3 ± 1.2	0.237 ± 0.02	75.7 ± 1.7
11	0	−1	+1	186 ± 3.3	+20.4 ± 0.9	0.251 ± 0.02	68.3 ± 1.5
12	0	+1	+1	222 ± 4.4	+29.8 ± 1.3	0.242 ± 0.02	77.9 ± 1.9
13	0	0	0	229 ± 4.7	+31.5 ± 1.4	0.218 ± 0.01	87.4 ± 2.3
14	0	0	0	231 ± 4.9	+30.9 ± 1.3	0.221 ± 0.01	86.8 ± 2.1
15	0	0	0	230 ± 4.6	+32.0 ± 1.5	0.215 ± 0.01	88.1 ± 2.4
16	0	0	0	230 ± 4.8	+31.2 ± 1.4	0.219 ± 0.01	87.2 ± 2.2
17	0	0	0	229 ± 4.5	+31.7 ± 1.5	0.217 ± 0.01	87.9 ± 2.5

3 Results and discussion

3.1 BBD experimental matrix and measured responses

The 17 formulations generated by the Box–Behnken design showed a wide range of measured responses, confirming that the three chosen factors had a meaningful impact on nanocomposite quality. Particle size ranged from 173 nm (run 5, low MOF ratio, low Fe_3O_4) to 269 nm (run 4, high MOF ratio, high chitosan). Zeta potential ranged from +18.7 mV (run 9) to +32.1 mV (run 4). PDI values ranged from 0.215 to 0.276. Encapsulation efficiency varied from 64.9% (run 9) to 88.1% (run 15), demonstrating that the central conditions produced the best drug loading. The five center-point replicates (runs 13–17) gave very similar results to each other (*e.g.*, EE% 86.8–88.1%), showing that the preparation method is reproducible. The full experimental matrix is shown in Table 2.

3.1.1 Statistical model fitting and ANOVA. The four fitted quadratic polynomial equations (coded values) derived from the Box–Behnken design are presented below. Each equation encapsulates the linear, interaction, and quadratic contributions of the three independent factors (X_1 = MOF-to-drug ratio; X_2 = chitosan concentration; X_3 = Fe_3O_4 content) to the respective response:

$$Y_1\,(\text{PS, nm}) = 230.00 + 32.38X_1 + 14.25X_2 + 8.21X_3 + 7.92X_1X_2 - 5.69X_1X_3 - 4.00X_2X_3 - 12.45X_1^2 - 8.48X_2^2 - 6.63X_3^2 \quad (12)$$

$$Y_2\,(\text{ZP, mV}) = +31.26 + 3.47X_1 + 4.00X_2 + 2.14X_3 + 1.78X_1X_2 - 1.31X_1X_3 - 0.90X_2X_3 - 3.26X_1^2 - 2.68X_2^2 - 1.93X_3^2 \quad (13)$$

$$Y_3\,(\text{PDI}) = 0.219 + 0.0292X_1 + 0.0217X_2 + 0.0125X_3 + 0.0092X_1X_2 + 0.0073X_1X_3 + 0.0045X_2X_3 - 0.0177X_1^2 - 0.0150X_2^2 - 0.0102X_3^2 \quad (14)$$

$$Y_4\,(\text{EE\%, \%}) = 87.48 + 8.84X_1 + 7.06X_2 + 3.20X_3 + 2.38X_1X_2 - 1.45X_1X_3 + 1.02X_2X_3 - 8.44X_1^2 - 4.67X_2^2 - 2.44X_3^2 \quad (15)$$

Each of the four responses was fitted to a second-order polynomial model. Table 3 presents all four ANOVA results side by side in a single collective table. All four models were statistically significant ($p < 0.0001$ for the model F-test) and showed a non-significant lack-of-fit ($p > 0.05$), which means the models fit the data well and can be trusted to make predictions. R^2 values were above 0.994 for all responses, and the difference between adjusted R^2 and predicted R^2 was less than 0.2 in all cases, confirming that the models are not over-fitted. Adequate precision values ranged from 38.7 to 54.3, all well above the minimum acceptable value of 4, indicating a strong signal-to-noise ratio and reliable model discrimination.

Among all factors, the MOF-to-drug ratio (X_1) had the largest effect on particle size and encapsulation efficiency,

Table 3 Collective ANOVA summary for all four quadratic response surface models. SS = sum of squares

Source	PS SS	p	ZP SS	p	PDI SS	p	EE% SS	p
Model	4821	<0.0001	152.8	<0.0001	0.00812	<0.0001	844.2	<0.0001
X_1	2105	<0.0001	48.26	<0.0001	0.00341	<0.0001	312.5	<0.0001
X_2	891	<0.0001	64.18	<0.0001	0.00188	<0.0001	198.8	<0.0001
X_3	312	0.0002	18.43	0.0038	0.00062	0.0091	41.23	0.0003
X_1X_2	249	0.0006	12.61	0.0112	0.00034	0.0248	22.56	0.0018
X_1X_3	129	0.0041	6.84	0.0418	0.00021	0.0631	8.41	0.0132
X_2X_3	64	0.0284	3.22	0.1124	0.00008	0.2840	4.18	0.0402
X_1^2	613	<0.0001	42.17	<0.0001	0.00124	0.0002	178.3	<0.0001
X_2^2	284	0.0003	28.64	0.0008	0.00089	0.0012	54.62	0.0001
X_3^2	175	0.0018	14.78	0.0078	0.00041	0.0182	23.63	0.0016
Residual	148	—	4.61	—	0.00031	—	4.19	—
Lack of fit	96	0.163	3.18	0.189	0.00019	0.201	2.84	0.178
Pure error	52	—	1.43	—	0.00012	—	1.35	—
R^2	0.9968		0.9941		0.9953		0.9951	
R_{adj}^2	0.9927		0.9866		0.9893		0.9888	
R_{pred}^2	0.9782		0.9614		0.9712		0.9741	
Adeq. prec	54.3		38.7		46.1		42.7	
CV%	0.84		1.12		1.43		1.03	

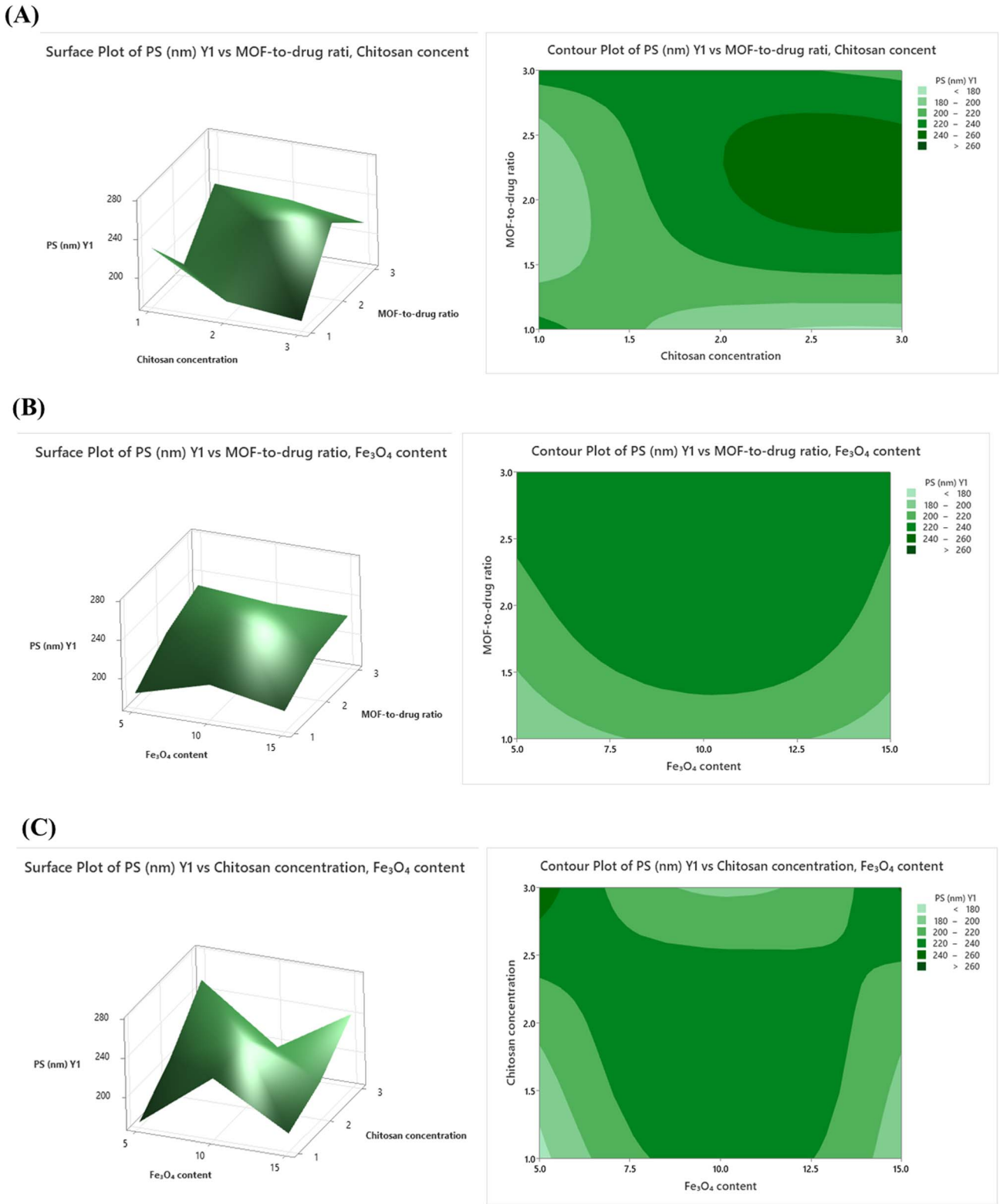

Fig. 1 Three-dimensional (3D) response surface and corresponding two-dimensional (2D) contour plots illustrating the combined effects of (A) MOF-to-drug ratio (X_1) and chitosan concentration (X_2), (B) MOF-to-drug ratio (X_1) and Fe_3O_4 content (X_3), and (C) chitosan concentration (X_2) and Fe_3O_4 content (X_3) on the particle size (Y_1, nm) of the Cur/Fe_3O_4@ZIF-8@CS nanocomposites. The third factor in each plot is held constant at its center-point level ($X_1 = 2:1$, $X_2 = 2.0$ mg mL^{-1}, $X_3 = 10\%$ w/w).

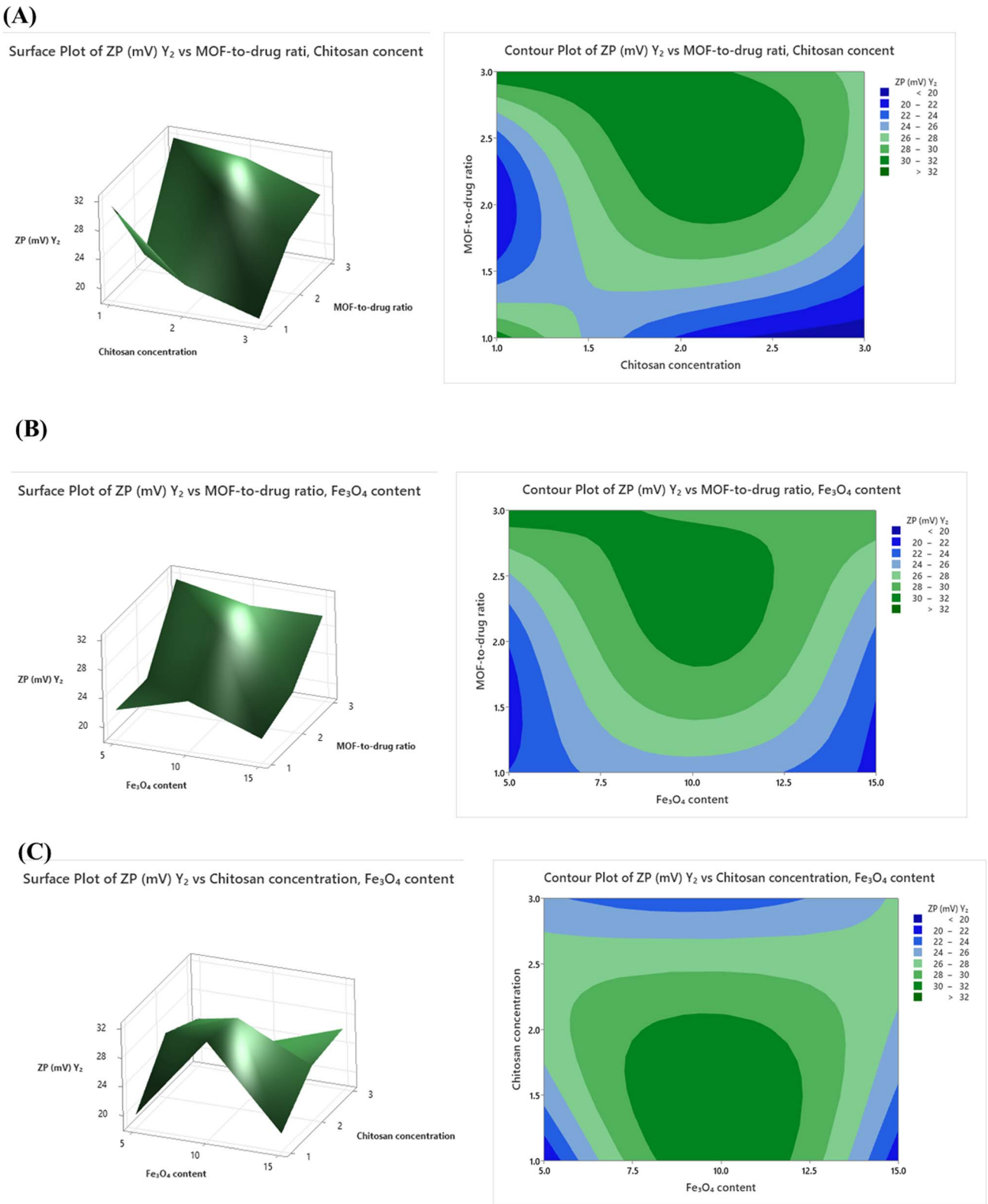

Fig. 2 Three-dimensional (3D) response surface and corresponding two-dimensional (2D) contour plots illustrating the combined effects of (A) MOF-to-drug ratio (X_1) and chitosan concentration (X_2), (B) MOF-to-drug ratio (X_1) and Fe_3O_4 content (X_3), and (C) chitosan concentration (X_2) and Fe_3O_4 content (X_3) on the zeta potential (Y_2, mV) of the Cur/Fe_3O_4@ZIF-8@CS nanocomposites. The third factor in each plot is held constant at its center-point level ($X_1 = 2:1$, $X_2 = 2.0$ mg mL^{-1}, $X_3 = 10\%$ w/w).

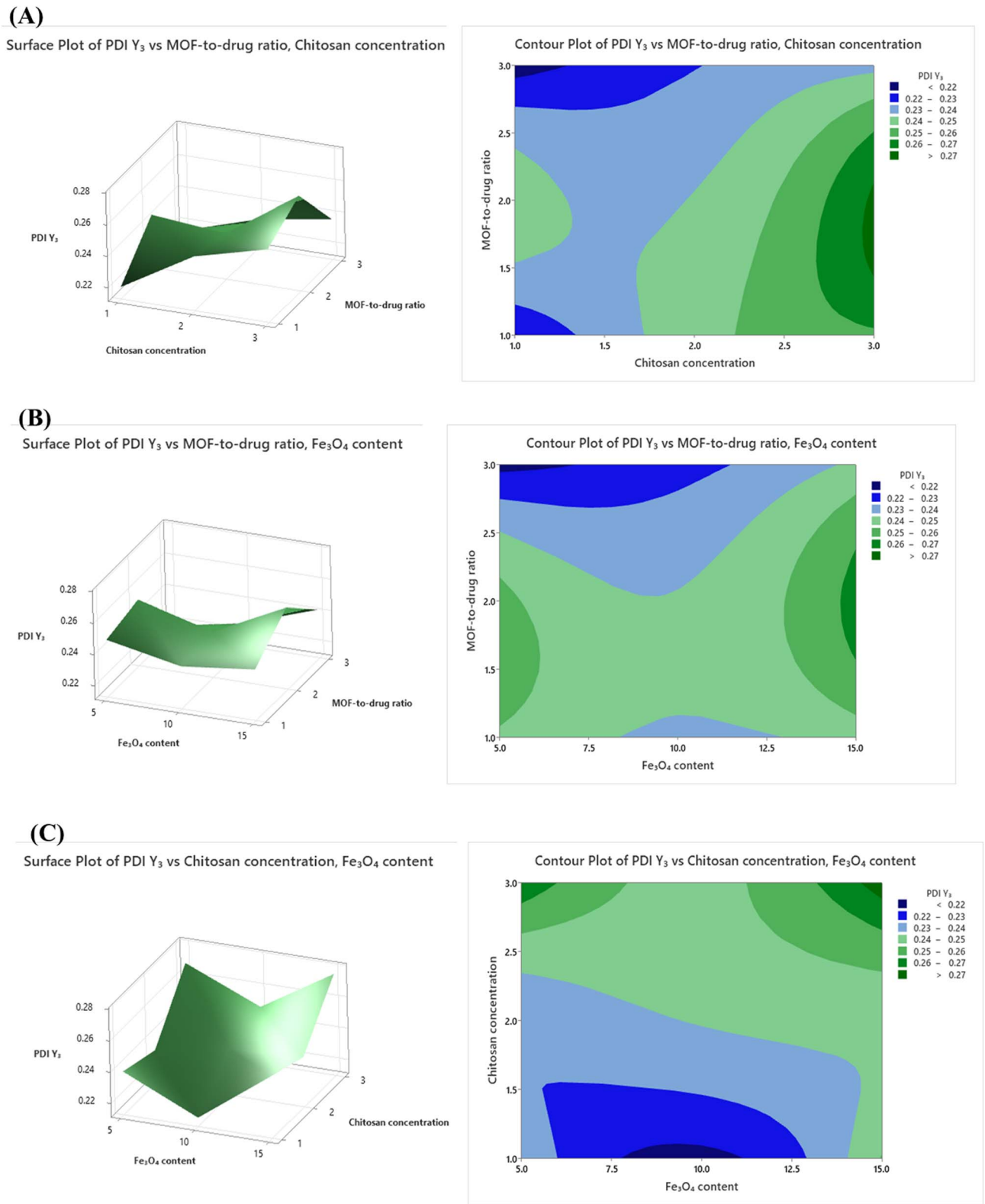

Fig. 3 Three-dimensional (3D) response surface and corresponding two-dimensional (2D) contour plots illustrating the combined effects of (A) MOF-to-drug ratio (X_1) and chitosan concentration (X_2), (B) MOF-to-drug ratio (X_1) and Fe_3O_4 content (X_3), and (C) chitosan concentration (X_2) and Fe_3O_4 content (X_3) on the polydispersity index (Y_3, PDI) of the Cur/Fe_3O_4@ZIF-8@CS nanocomposites. The third factor in each plot is held constant at its center-point level ($X_1 = 2:1$, $X_2 = 2.0$ mg mL^{-1}, $X_3 = 10\%$ w/w).

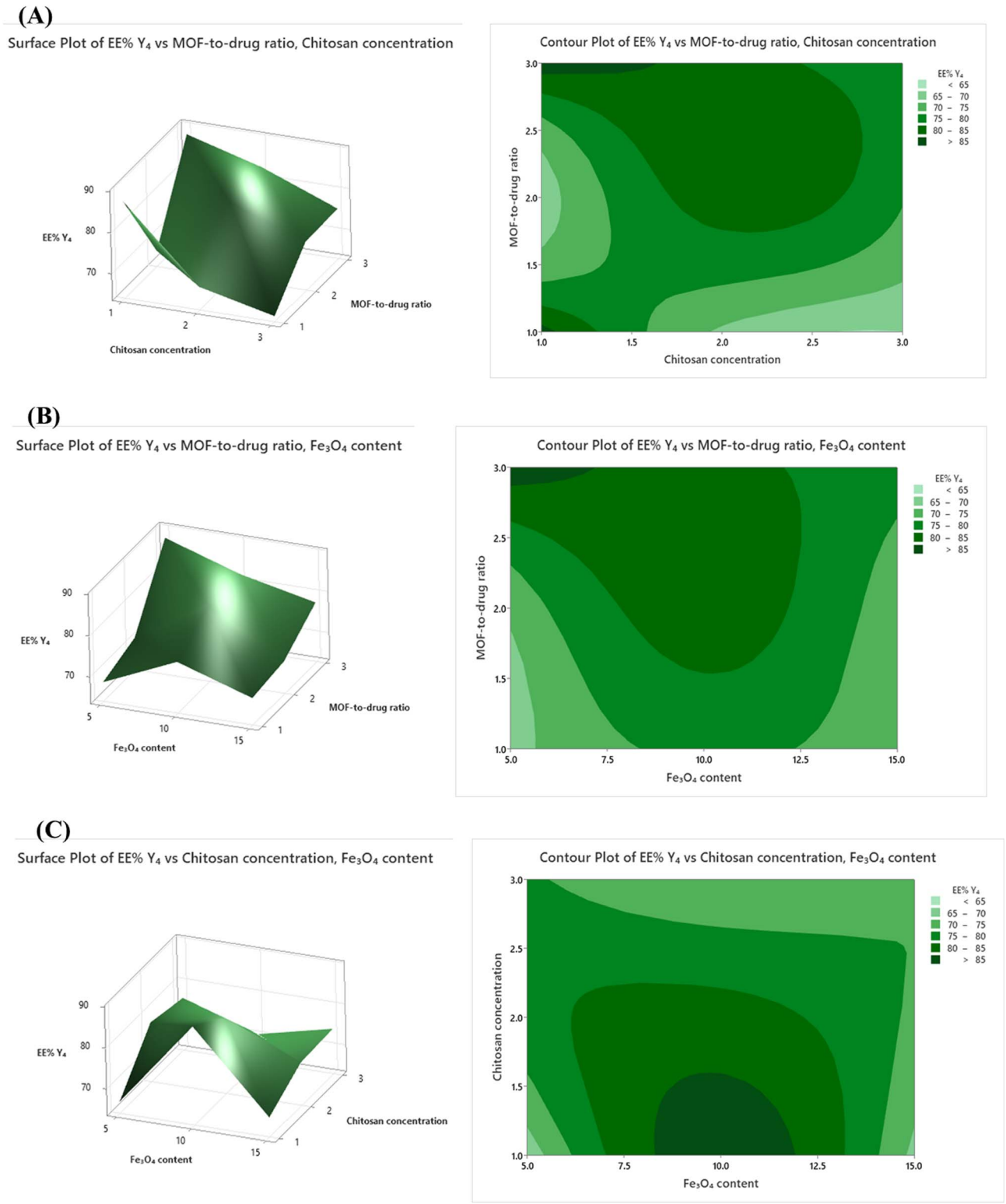

Fig. 4 Three-dimensional (3D) response surface and corresponding two-dimensional (2D) contour plots illustrating the combined effects of (A) MOF-to-drug ratio (X_1) and chitosan concentration (X_2), (B) MOF-to-drug ratio (X_1) and Fe_3O_4 content (X_3), and (C) chitosan concentration (X_2) and Fe_3O_4 content (X_3) on the encapsulation efficiency (Y_4, %) of the Cur/Fe_3O_4@ZIF-8@CS nanocomposites. The third factor in each plot is held constant at its center-point level ($X_1 = 2:1$, $X_2 = 2.0$ mg mL^{-1}, $X_3 = 10\%$ w/w).

while chitosan concentration (X_2) was the strongest driver of zeta potential. PDI was most affected by X_1 as well, suggesting that higher MOF-to-drug ratios introduce some size heterogeneity, possibly because multiple iron oxide cores can become embedded within a single ZIF-8 crystal at higher ratios.

Table 4 Model-predicted *versus* experimentally measured quality attributes for the optimized formulation ($X_1 = 2:1$; $X_2 = 2.0$ mg mL; $X_3 = 10\%$ w/w; $n = 3$, mean ± SD)

Response	Predicted value	Measured value ($n = 3$, mean ± SD)	Error (%)
Particle size (nm) [DLS, hydrodynamic diameter]	232	228.6 ± 4.7	1.51
Zeta potential (mV)	+30.8	+31.5 ± 1.4	2.27
PDI	0.218	0.218 ± 0.01	0.00
Encapsulation eff. (%)	87.1	87.4 ± 2.3	0.34

Table 5 Physicochemical properties of the nanocomposite at each step of the preparation process

Parameter	Fe_3O_4 MNPs	Fe_3O_4@ZIF-8/Cur	Final nanocomposite
Hydrodynamic size (nm)	28.3 ± 2.4	186.3 ± 3.9	228.6 ± 4.7
TEM core size (nm)	10.3 ± 1.4	142.7 ± 8.6	~220
PDI	0.171 ± 0.01	0.231 ± 0.02	0.218 ± 0.01
Zeta potential (mV)	−14.2 ± 1.2	+18.6 ± 1.4	+31.5 ± 1.4
Encapsulation efficiency (%)	—	79.2 ± 1.9	87.4 ± 2.3
Drug loading (%)	—	7.31 ± 0.18	8.08 ± 0.21
Saturation magnetization (emu g^{-1})	62.8	—	6.97

3.1.2 Effect of formulation factors on each response. Particle size (Y_1) increased with both X_1 (MOF-to-drug ratio) and X_2 (chitosan concentration), as illustrated by the steep slopes in the 3D response surface and the curved contour lines in Fig. 1A–C. Higher MOF-to-drug ratios require a larger ZIF-8 crystal to accommodate more drug molecules, and thicker chitosan layers naturally add to the overall particle diameter. The negative quadratic terms for both X_1 and X_2 show that the effect of each factor levels off at higher levels, with an apparent size maximum within the design space.

Zeta potential (Y_2) was most strongly influenced by X_2 (Fig. 2A–C). As chitosan concentration increased, more positively charged polymer chains coated the surface, raising the zeta potential from around +19 mV to +32 mV. This is a desirable outcome because higher zeta potential improves colloidal stability and enhances the interaction of the nanoparticle with negatively charged bacterial cell membranes.

PDI (Y_3) increased with X_1 and X_3 (Fe_3O_4 content), a trend that can be observed in Fig. 3A–C. Larger amounts of magnetic nanoparticles may create some variation in the number of cores per ZIF-8 particle, leading to a broader size distribution. However, all PDI values remained below 0.28, staying within acceptable limits for nanoparticles.

Encapsulation efficiency (Y_4) increased with X_1 but followed a curved (quadratic) relationship (Fig. 4A–C). EE% improved as the MOF framework increased relative to drug, because more pore space was available for curcumin to occupy. However, at the highest MOF-to-drug ratios, EE% began to plateau and slightly decline, likely because the pores became partially blocked or the drug distribution became inefficient. The highest EE% values (86.8–88.1%) were found consistently at the center-point conditions.

3.1.3 Optimization and verification. The desirability function in Minitab® v21.0 was used to find the single best formulation that simultaneously achieved good results across all four responses: small particle size, high zeta potential, low PDI, and high EE%. The optimal formulation identified was: $X_1 = 2:1$ (MOF : drug), $X_2 = 2.0$ mg per mL chitosan, $X_3 = 10\%$ Fe_3O_4. This formulation was then prepared three times independently to check whether the predicted values matched the actual measured values. As shown in Table 4, the measured results agreed very closely with the model predictions, with errors of less than 2.3% for all four responses. This confirms that the Box–Behnken model is valid and that the optimized formulation can be reproduced reliably. All particle size values reported in the Box–Behnken design and optimization (predicted: 232 nm; measured: 228.6 ± 4.7 nm) refer to the hydrodynamic diameter as determined by DLS, which is the standard physicochemical quality attribute applied in pharmaceutical quality by design frameworks. These values are not directly comparable to TEM core dimensions, which are systematically smaller due to the absence of the hydration shell and chitosan corona under dry imaging conditions (see Sections 3.2.1 and 3.2.2).

3.2 Physicochemical characterization

3.2.1 Particle size, PDI, and zeta potential across preparation steps. Particle size and surface charge were tracked at three stages: bare Fe_3O_4 nanoparticles, the intermediate core–shell particles (Fe_3O_4@ZIF-8/Cur), and the final chitosan-coated nanocomposite. The results are summarized in Table 5. Bare Fe_3O_4 particles measured 28.3 ± 2.4 nm by DLS (TEM core size: 10.3 ± 1.4 nm; the difference reflects the hydration shell present around the particle in aqueous suspension, which is captured by DLS but collapses entirely under the high-vacuum conditions of TEM). After ZIF-8 crystallization around the magnetic cores, the hydrodynamic diameter increased substantially to 186.3 ± 3.9 nm (TEM core size: 142.7 ± 8.6 nm), confirming that a thick porous ZIF-8 shell had formed around the iron oxide cores. This magnitude of hydrodynamic size increase following ZIF-8 shell

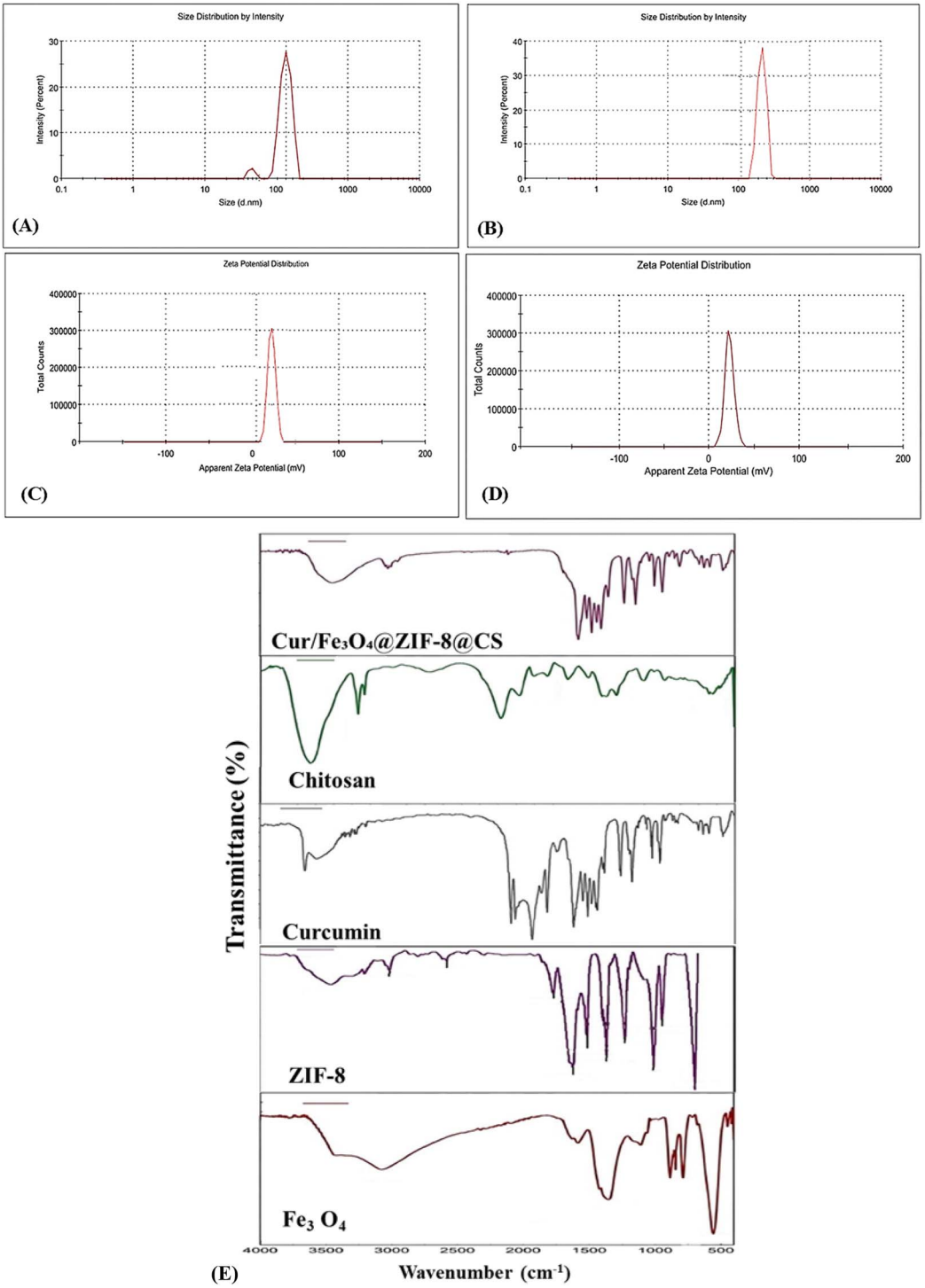

Fig. 5 DLS characterization of the nanocomposite at successive preparation stages. (A) Hydrodynamic size distribution of the intermediate Fe_3O_4@ZIF-8/Cur particles prior to chitosan coating (186.3 ± 3.9 nm, PDI 0.231 ± 0.02), confirming successful ZIF-8 shell formation around the Fe_3O_4 cores. (B) Hydrodynamic size distribution of the final Cur/Fe_3O_4@ZIF-8@CS nanocomposite after chitosan coating (228.6 ± 4.7 nm, PDI 0.218 ± 0.01); the ~42 nm size increment relative to (A) is consistent with deposition of the chitosan polymer layer. (C) Zeta potential distribution of Fe_3O_4@ZIF-8/Cur before chitosan coating (+18.6 ± 1.4 mV). (2D) Zeta potential distribution of Cur/Fe_3O_4@ZIF-8@CS after chitosan coating (+31.5 ± 1.4 mV), demonstrating a +12.9 mV shift that unambiguously confirms chitosan surface adsorption and enhanced colloidal stability. (E) FTIR spectra of Fe_3O_4, ZIF-8, chitosan, curcumin, and the optimized Cur/Fe_3O_4@ZIF-8@CS nanocomposite. The nanocomposite retained the characteristic Fe–O bands (565 and 397 cm^{-1}), confirming preservation of the magnetic core, while ZIF-8 bands (Zn–N and C═N) appeared with slight shifts, indicating framework integrity. The broadened O–H/N–H band and shifted amide I peak (1632 cm^{-1}) confirmed chitosan coating. A downshift of the curcumin C═O/C═C band (~1626 → 1606 cm^{-1}) and attenuation of the phenolic O–H band indicated host–guest interactions and successful curcumin encapsulation.

Table 6 Summary of key FTIR bands for individual components and final nanocomposite[a]

Assignment	Fe_3O_4 (cm^{-1})	ZIF-8 (cm^{-1})	Chitosan (cm^{-1})	Nanocomposite (cm^{-1})
Fe–O stretching	569, 399	—	—	565, 397 (retained)
Zn–N coordination	—	421	—	418 (shifted)
C=N stretching (imidazolate)	—	1584	—	1578 (shifted)
N–H/O–H stretch (chitosan)	—	—	3348	3338 (broadened)
Amide I (C=O, chitosan)	—	—	1648	1632 (red-shifted)
C–O–C glycosidic (chitosan)	—	—	1025	1022 (retained)
C=O/C=C conjugated (curcumin, β-diketone)	—	—	—	1606 (red-shifted from 1626)
O–H enol stretch (curcumin)	—	—	—	3505 (attenuated)

[a] All wavenumbers are approximate (±2 cm^{-1}). Dashes indicate absence of the band in the respective individual component.

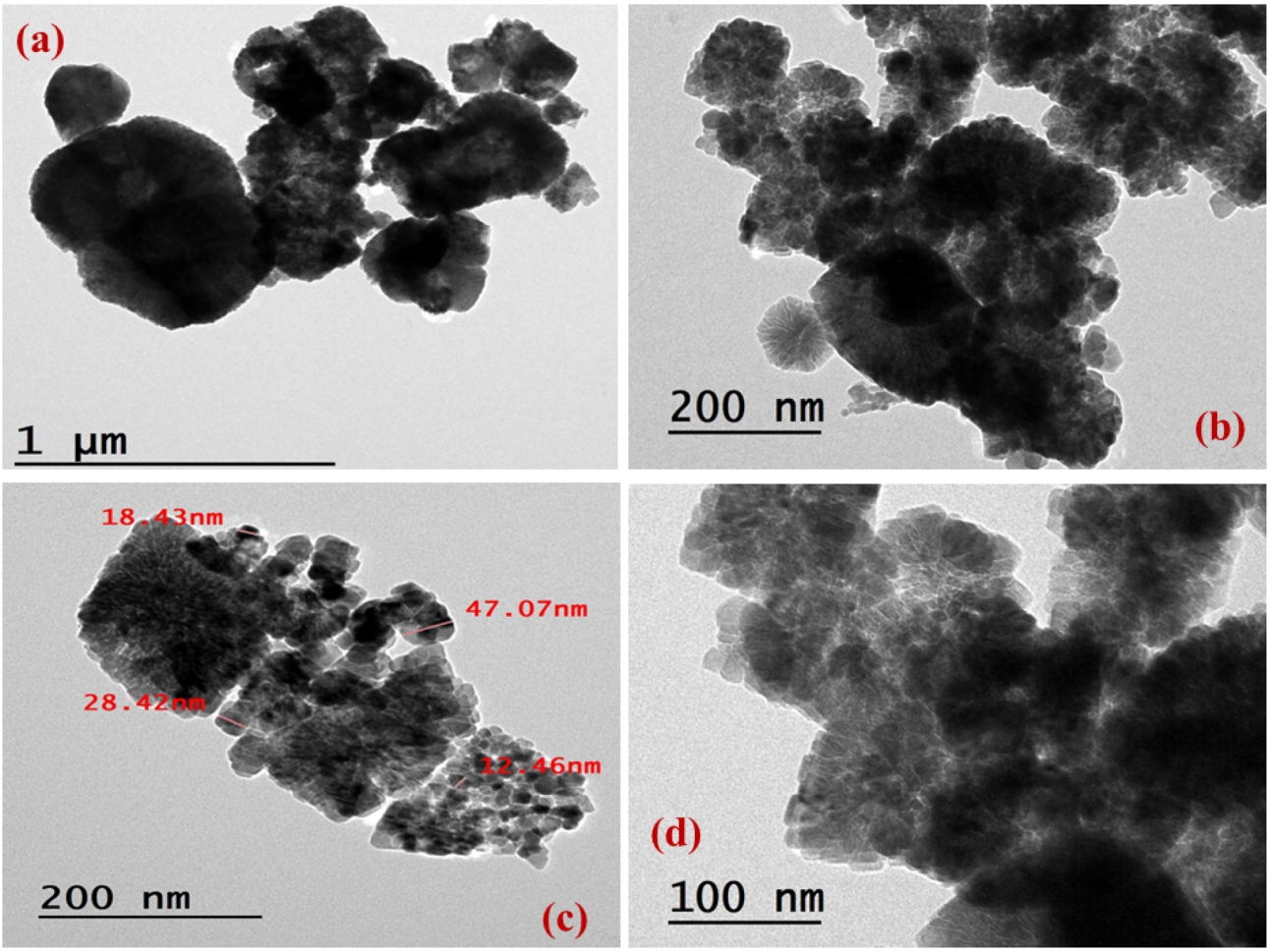

Fig. 6 TEM images of the optimized Cur/Fe_3O_4@ZIF-8@CS nanocomposite at increasing magnifications. (a) Low magnification (1 μm) showing irregularly aggregated clusters; dense dark regions correspond to Fe_3O_4 cores. (b) Intermediate magnification (200 nm) revealing the core–shell architecture: electron-dense Fe_3O_4 cores surrounded by the lighter ZIF-8 framework and chitosan coating, with characteristic ZIF-8 flower-like crystalline features at aggregate peripheries. (c) Higher magnification (200 nm) with annotated crystallite dimensions (12.46–47.07 nm), representing dry Fe_3O_4 and ZIF-8 sub-unit sizes; these are smaller than the DLS hydrodynamic diameter (228.6 ± 4.7 nm) due to collapse of the hydrated chitosan corona under vacuum. (d) Highest magnification (100 nm) confirming the porous ZIF-8 shell, multiple Fe_3O_4 cores per ZIF-8 crystal, and a diffuse chitosan surface layer, collectively verifying successful nanocomposite assembly.

formation around Fe_3O_4 cores is well-documented; Ettlinger *et al.*[41] and Kong *et al.*[42] both reported comparable dimensional transitions from ~20–30 nm magnetic cores to ~120–180 nm ZIF-8 core–shell particles under analogous room-temperature synthesis conditions, fully consistent with our observed increase from 28.3 to 186.3 nm. The systematic discrepancy

between DLS hydrodynamic diameter (186.3 nm) and TEM core size (142.7 nm) at this intermediate stage reflects the collapse of the hydrated ZIF-8 organic linker network under TEM vacuum conditions, a phenomenon specifically documented by Mittal *et al.*[34] for ZIF-8 nanoparticle systems. After chitosan coating, the hydrodynamic diameter increased further to 228.6 ± 4.7 nm, with a corresponding TEM core size of approximately 220 nm, and the zeta potential changed from +18.6 mV (ZIF-8 surface) to +31.5 mV; a +12.9 mV shift that unambiguously confirms successful chitosan deposition onto the particle surface as shown in Fig. 5A–D.

This step-by-step hydrodynamic size increase combined with the charge reversal pattern is strong evidence that each layer was added successfully. The final PDI of 0.218 shows the particles are fairly uniform in size. The zeta potential of +31.5 mV is well above the +20 mV stability threshold, meaning the particles will stay dispersed in solution without clumping together. When stored as a freeze-dried powder and redispersed, the particles retained their size and PDI for at least 90 days at 4 °C, confirming good physical stability.

It is important to note that the hydrodynamic diameters measured by DLS (186.3 nm for Fe_3O_4@ZIF-8/Cur and 228.6 nm for the final nanocomposite) are consistently larger than the corresponding TEM core sizes, as expected. DLS measures the full hydrodynamic envelope of the particle in suspension, including the chitosan corona and the surrounding electrical double layer, whereas TEM captures only the dry inorganic/polymeric core under vacuum. This discrepancy is well established for polymer-coated nanoparticles and is not an inconsistency; both measurement techniques provide complementary and consistent information about different structural dimensions of the same particle.[34,35,41–44]

3.2.2 FTIR spectroscopic characterization. To confirm the successful assembly of Cur/Fe_3O_4@ZIF-8@CS, Fourier-transform infrared (FTIR) spectra were recorded for each individual component (bare Fe_3O_4 nanoparticles, pure ZIF-8, free chitosan, and free curcumin) and for the final nanocomposite powder using an ATR-FTIR spectrometer (Bruker Alpha II, Germany) over the wavenumber range 400–4000 cm^{-1}. All key bands are summarized in Table 6.

The spectrum of bare Fe_3O_4 displayed two characteristic Fe–O stretching vibrations at approximately 569 cm^{-1} and 399 cm^{-1}, consistent with the inverse spinel lattice vibrations of magnetite reported in the literature.[45,46] A broad O–H absorption around 3420 cm^{-1} was also present, attributable to surface hydroxyl groups and adsorbed moisture on the nanoparticle surface. Both Fe–O bands were retained in the final nanocomposite spectrum, confirming that the magnetic iron oxide core was structurally preserved throughout the multi-step fabrication process.

The FTIR spectrum of as-synthesized ZIF-8 showed the following characteristic bands: a Zn–N coordination stretching vibration at 421 cm^{-1}, out-of-plane bending of the imidazole ring at 690–760 cm^{-1}, in-plane bending of C–H at 950–1200 cm^{-1}, C–N stretching of the imidazolate linker at 1145–1180 cm^{-1}, C=N stretching at 1584 cm^{-1}, and aromatic C–H stretching at 3135 cm^{-1}. These bands are in excellent agreement with published ZIF-8 reference spectra.[12,34] In the nanocomposite, the Zn–N and C=N bands were retained but shifted slightly to 418 cm^{-1} and 1578 cm^{-1} respectively, indicating that the ZIF-8 framework remained intact while undergoing mild coordination perturbation upon interaction with the iron oxide surface and chitosan coating.

The spectrum of free low-molecular-weight chitosan exhibited a broad O–H/N–H stretching envelope centered at 3348 cm^{-1}, aliphatic C–H stretching at 2873 cm^{-1}, a carbonyl band (amide I, C=O) at 1648 cm^{-1}, N–H bending (amide II) at 1590 cm^{-1}, and a C–O–C glycosidic linkage stretching band at 1025 cm^{-1}. These features are consistent with the established FTIR fingerprint of partially deacetylated chitosan.[17] In the nanocomposite spectrum, the O–H/N–H band was retained but broadened, and the amide I band shifted to 1632 cm^{-1}. This red-shift is consistent with the formation of hydrogen bonds between chitosan amine groups and the surface oxygen atoms of Fe_3O_4 and/or the imidazolate linkers of ZIF-8, confirming chitosan surface deposition.[35,47]

The FTIR spectrum of curcumin showed characteristic bands at 3510 cm^{-1} (O–H stretch of enol form), 3008 cm^{-1} (aromatic C–H stretch), 1626 cm^{-1} (C=O/C=C conjugated stretch, β-diketone chelated form), 1510 cm^{-1} (C=C aromatic ring stretch), 1270 cm^{-1} (C–O–C phenolic ether), and 960 cm^{-1} (=C–H bending). These are in full agreement with established curcumin reference spectra.[20,31]

The FTIR spectrum of the optimized nanocomposite (Cur/Fe_3O_4@ZIF-8@CS) showed the following critical features confirming successful multicomponent integration: retention of Fe–O bands at ~565 and ~397 cm^{-1} which confirms preservation of the Fe_3O_4 magnetic core within the nanocomposite; retention of ZIF-8 Zn–N and C=N bands (shifted to 418 and 1578 cm^{-1}) which confirms ZIF-8 framework formation and mild coordination interaction with surrounding components; presence of chitosan amide I and glycosidic bands (shifted amide I at 1632 cm^{-1}) which confirms successful chitosan coating and hydrogen-bond interaction with the ZIF-8/Fe_3O_4 surface; shift of curcumin C=O/C=C conjugated band from 1626 to 1606 cm^{-1} where this bathochromic shift is a strong indicator of host–guest interaction between encapsulated curcumin and the ZIF-8 pore environment. The downshift is consistent with weakening of the C=O bond through π–π stacking interactions between the aromatic rings of curcumin and the imidazolate linkers, as well as possible hydrogen bonding of the curcumin enol O–H with the Zn–N coordination sites inside the MOF pore.[12,34] This confirms that curcumin is encapsulated within the ZIF-8 pores and not merely adsorbed on the outer particle surface; attenuation of the free curcumin O–H band at 3510 cm^{-1}: the reduction in intensity of the free enol O–H stretch in the nanocomposite spectrum relative to pure curcumin is consistent with involvement of this group in hydrogen bonding within the ZIF-8 cage, further supporting genuine encapsulation.

Taken together, the FTIR data shown in Fig. 5E provide comprehensive spectroscopic confirmation that all four components including Fe_3O_4, ZIF-8, chitosan, and curcumin are present in the final nanocomposite and that the assembly

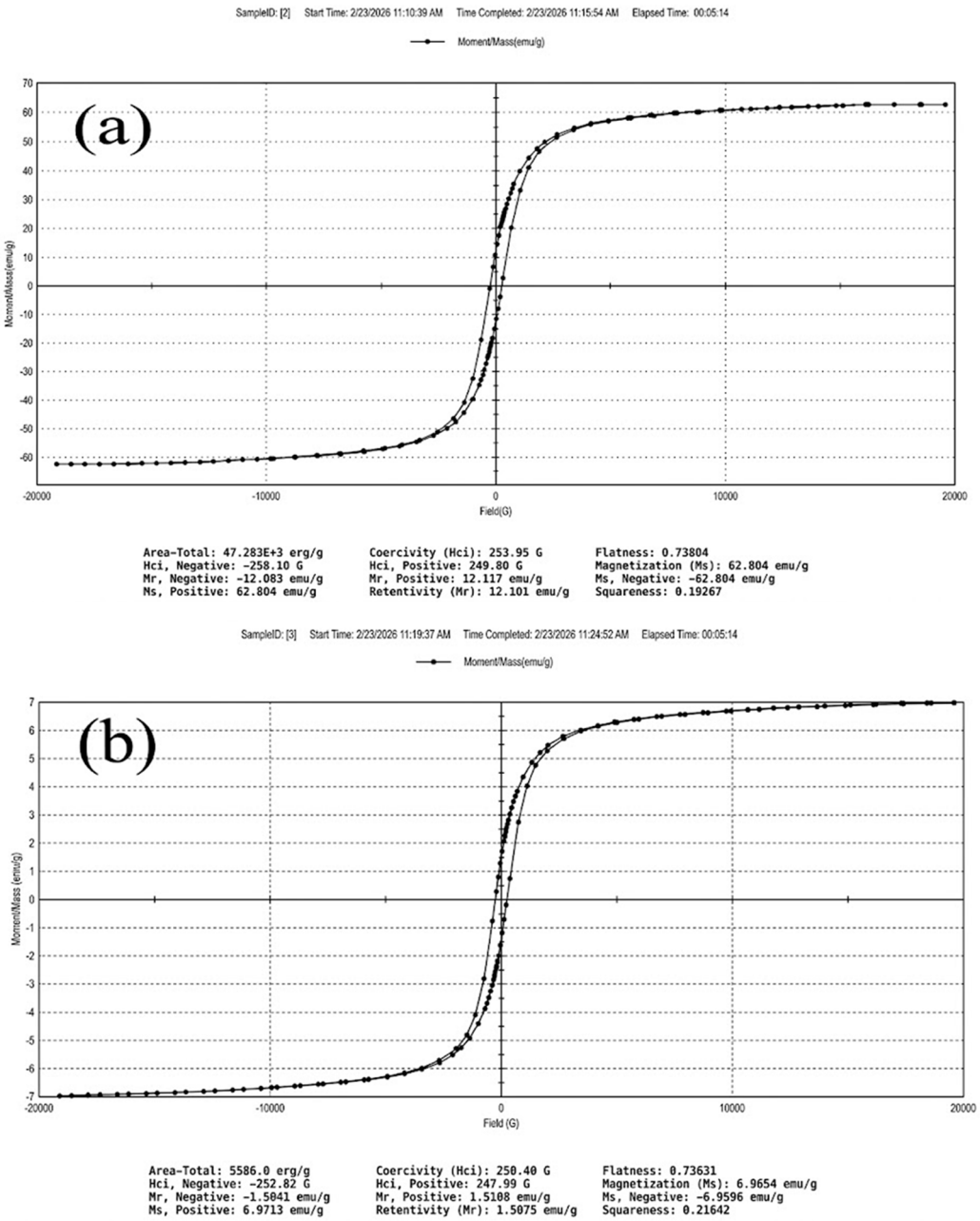

Fig. 7 VSM hysteresis loops at room temperature for (a) bare Fe_3O_4 nanoparticles ($M_s = 62.8$ emu g^{-1}, $H_{ci} = 253.95$ G, $M_r = 12.10$ emu g^{-1}) and (b) Cur/Fe_3O_4@ZIF-8@CS nanocomposite ($M_s = 6.97$ emu g^{-1}, $H_{ci} = 250.40$ G, $M_r = 1.51$ emu g^{-1}). Both samples show near-superparamagnetic S-shaped loops with low coercivity and squareness <0.5, confirming soft magnetic behavior with negligible remanence. The decrease in M_s from (a) to (b) reflects dilution of the Fe_3O_4 phase by the non-magnetic ZIF-8, chitosan, and curcumin components, while near-identical coercivity values confirm that the magnetic character of the Fe_3O_4 cores is retained after composite assembly.

involved real chemical/physical interactions between components rather than mere physical mixing. This is fully consistent with the step-by-step size and zeta potential evolution documented in Table 5 and the TEM images in Fig. 6.

3.2.3 Transmission electron microscopy. HRTEM imaging further confirmed the successful formation of the hybrid nanocomposite, revealing the co-existence of Fe_3O_4 magnetic cores integrated within the ZIF-8 MOF framework, surrounded by the chitosan coating and encapsulated curcumin (Fig. 6a–d). The oxide cores appear as irregular, densely packed dark regions attributable to their higher electron density relative to the surrounding organic components.[46] The lighter, semi-transparent surrounding matrix corresponds to the chitosan shell and the ZIF-8 porous framework, within which curcumin is encapsulated.[48] Individual crystallite cross-sections within the composite range from approximately 12.46 to 47.07 nm, consistent with the sub-unit dimensions of the Fe_3O_4 cores and nascent ZIF-8 crystallites; the overall morphology reflects an

irregular, aggregated architecture rather than discrete monodisperse spheres. The darker core regions are fully consistent with Fe_3O_4 electron density, while the relatively lighter surrounding matrix is attributable to the low-density chitosan layer and ZIF-8 organic linker network.[47] The observed aggregation is an expected outcome of the strong magnetic dipole–dipole interactions between Fe_3O_4 nanoparticles and their surface interactions with chitosan and ZIF-8 components during composite assembly, as previously reported for analogous magnetic MOF nanocomposites.[49] Despite this aggregation, the overall particle distribution remains relatively uniform, and the colloidal stability measured by DLS (PDI = 0.218) confirms that the composite retains an acceptably narrow size distribution in suspension. The observed size range of individual crystallites, the core–shell contrast pattern, and the aggregated cluster behavior together support the conclusion that chitosan acts as a stabilizing and binding agent bridging the Fe_3O_4 cores and the ZIF-8 framework, while ZIF-8 contributes structural support and the porous network responsible for curcumin encapsulation.[48,49]

3.2.4 Magnetic properties. The magnetic behavior of bare Fe_3O_4 nanoparticles and the final Cur/Fe_3O_4@ZIF-8@CS nanocomposite was evaluated by VSM at room temperature, and the resulting hysteresis loops are presented in Fig. 7a and b, respectively. Both samples displayed the characteristic S-shaped hysteresis loop with negligible remanence and low coercivity, confirming near-superparamagnetic soft magnetic behavior at room temperature.

For the bare Fe_3O_4 nanoparticles (Fig. 7a), the saturation magnetization was $M_s = 62.8$ emu g^{-1}, with a coercivity of $H_{ci} =$ 253.95 G and retentivity of $M_r = 12.10$ emu g^{-1} (squareness $M_r/M_s = 0.193$). The M_s value is lower than that of bulk magnetite (~92 emu g^{-1}), which is expected for nanoscale Fe_3O_4 particles and is attributable to surface spin disorder effects that is at the nanoscale, a significant proportion of iron atoms reside at the particle surface where coordination is incomplete, reducing the net magnetic moment per unit mass.[45] The low coercivity and squareness well below 0.5 confirm that the particles are in a near-superparamagnetic regime, meaning they respond strongly to an applied magnetic field but retain only minimal residual magnetization once the field is removed; a highly desirable property for biomedical applications where particle aggregation in the bloodstream must be avoided.[13]

After incorporation into the final Cur/Fe_3O_4@ZIF-8@CS nanocomposite (Fig. 7b), the saturation magnetization decreased substantially to $M_s = 6.97$ emu g^{-1}, with coercivity H_{ci} = 250.40 G and retentivity $M_r = 1.51$ emu g^{-1} (squareness = 0.216). This reduction in M_s is a direct and expected consequence of dilution of the magnetic Fe_3O_4 phase by the non-magnetic components including ZIF-8 framework, chitosan coating, and encapsulated curcumin which collectively constitute the majority of the composite mass and contribute no magnetic moment.[49] Importantly, the near-identical coercivity values between the bare Fe_3O_4 (253.95 G) and the final composite (250.40 G) confirm that the magnetic character of the iron oxide cores is fully preserved after coating, and that the ZIF-8 and chitosan layers do not alter the intrinsic magnetic domain structure of the Fe_3O_4 cores. Despite the lower absolute M_s, the composite retains sufficient magnetic responsiveness for external magnetic field-guided targeting, consistent with previously reported thresholds for magnetically steerable drug delivery nanocarriers.[13]

3.2.5 Encapsulation efficiency and drug loading. The optimized formulation achieved an encapsulation efficiency of 87.4 ± 2.3% and drug loading of 8.08 ± 0.21%. The EE% is modestly higher than that measured at the intermediate Fe_3O_4@ZIF-8/Cur stage prior to chitosan coating (79.2 ± 1.9%; Table 5). This increase is attributed to the chitosan coating layer physically sealing the ZIF-8 pore apertures and retaining curcumin molecules that would otherwise leach into the washing medium during the repeated centrifugation–washing cycles required at the intermediate stage; the final EE% measurement is therefore performed after this loss pathway has been closed by the polymer coating.[48] Both values are considerably higher than what is typically reported for conventional polymer-only nanoparticles (usually 40–70% EE%), and are attributed to the large internal surface area and pore volume of the ZIF-8 framework. The pores provide many sites for curcumin molecules to bind through interactions with the imidazolate linkers, holding the drug securely until the acidic environment triggers ZIF-8 degradation and drug release.

3.3 *In vitro* drug release

Fig. 8 shows the cumulative release profiles of free curcumin and the optimized nanocomposite at pH 5.5 and pH 7.4 over 72 hours. The results clearly show three important differences between the two systems.

First, free curcumin released very quickly in the first 30 minutes, giving 32.4 ± 1.2% release at pH 5.5 and 18.6 ± 0.9%

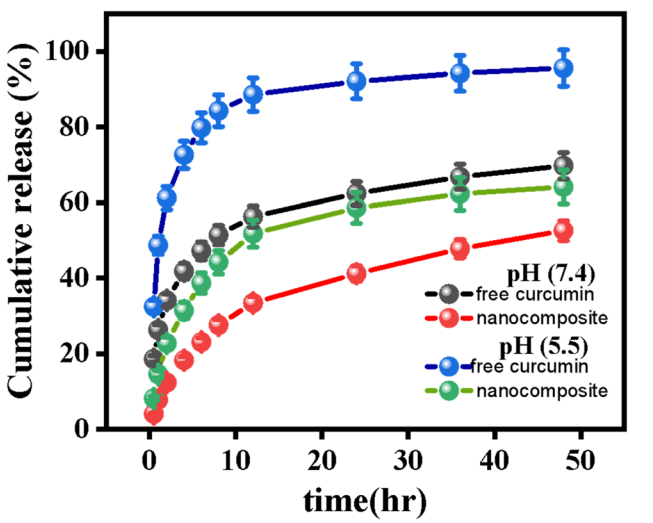

Fig. 8 Cumulative *in vitro* release of free curcumin and the optimized MOF–chitosan nanocomposite at pH 5.5 and 7.4 over 72 h. Free curcumin showed rapid burst release and early plateau, whereas the nanocomposite exhibited reduced initial release and sustained drug delivery. The nanocomposite also displayed higher release at pH 5.5 than at pH 7.4, confirming pH-responsive behavior.

Table 7 Kinetic model fitting parameters for free curcumin and the optimized nanocomposite at pH 5.5 and pH 7.4. Best-fit model selected by highest R^2 and lowest AIC

Parameter	Free Cur pH 5.5	Nanocomp. pH 5.5	Free Cur pH 7.4	Nanocomp. pH 7.4	Key finding
Zero-order (R^2)	0.889	0.942	0.861	0.918	Poor fit for free drug
Zero-order K_0 (% h^{-1})	1.12	3.21	0.89	1.47	Slower constant rate
First-order (R^2)	0.914	0.961	0.888	0.939	Improved for nanocomp.
First-order K_1 (h^{-1})	0.082	0.038	0.051	0.019	2–3× slower release
Higuchi (R^2)	0.961	0.987	0.937	0.974	Best fit for free drug
Higuchi K_H (% $h^{-1/2}$)	14.3	8.92	9.8	5.43	Sustained diffusion
Korsmeyer–Peppas (R^2)	0.976	0.994	0.958	0.981	Best fit: nanocomp.
K_P rate constant k	0.214	0.082	0.148	0.049	Controlled release
K_P exponent n	0.38	0.61	0.41	0.53	Non-Fickian transport
Release mechanism	Fickian	Anomalous	Fickian	Anomalous	Matrix + diffusion
Best-fit model	Higuchi	Korsmeyer–Peppas	Higuchi	Korsmeyer–Peppas	—

Table 8 Zone of inhibition (mm), MIC (μg mL^{-1}), and MBC/MFC (μg mL^{-1}) of Fe_3O_4@ZIF-8@CS and Cur/Fe_3O_4@ZIF-8@CS against five clinical microbial strains (mean ± SD, $n = 3$)[a]

Organism	ZOI (mm) blank NC	ZOI (mm) Cur-NC	ZOI (mm) free Cur	MIC (μg mL^{-1}) blank NC	MIC (μg mL^{-1}) Cur-NC	MIC (μg mL^{-1}) free Cur	MBC/MFC blank NC	MBC/MFC Cur-NC
S. agalactiae	16.00 ± 2.00^{aB}	20.00 ± 2.00^{aA}	8.33 ± 1.53	41.70 ± 18.01^{c}	11.07 ± 3.93^{c}	750 ± 62.5	162.53 ± 153.48	62.47 ± 54.16
S. aureus	15.33 ± 1.53^{abB}	18.67 ± 3.60^{abA}	7.67 ± 1.15	46.00 ± 28.06^{c}	18.57 ± 11.54^{c}	500 ± 46.9	72.93 ± 47.71	52.10 ± 18.01
E. coli	12.00 ± 2.00^{abB}	14.67 ± 3.06^{bA}	NI	13.33 ± 3.93^{c}	13.33 ± 3.92^{c}	>1000	145.83 ± 59.47	104.17 ± 36.05
K. pneumoniae	10.67 ± 3.06^{bB}	14.67 ± 3.06^{bA}	NI	104.17 ± 36.08^{a}	104.17 ± 36.08^{a}	>1000	104.17 ± 36.08	104.17 ± 36.08
C. albicans	11.33 ± 5.33^{abB}	18.67 ± 3.06^{abA}	6.67 ± 2.08	83.33 ± 36.08^{ab}	83.33 ± 36.08^{b}	875 ± 72.9	83.33 ± 36.08	83.33 ± 36.08

[a] NC = nanocomposite; Blank NC = Fe_3O_4@ZIF-8@CS; Cur-NC = Cur/Fe_3O_4@ZIF-8@CS; free Cur = free curcumin in 0.5% DMSO (v/v); NI = no measurable inhibition zone. Superscripts (a–c) within column: significant differences between microbial species ($p < 0.05$); (A and B) within row: significant differences between treatments ($p < 0.05$).

at pH 7.4. This early burst is a known problem with freely dissolved drugs; without any carrier to hold them back, they diffuse rapidly into the surrounding medium. By contrast, the nanocomposite released only 8.2 ± 0.4% at pH 5.5 and 4.1 ± 0.2% at pH 7.4 at the same time point. This much smaller burst shows that the MOF–chitosan structure successfully slows down initial drug escape.

Second, free curcumin reached a high release level quickly and then levelled off by 24 h, reaching about 92% at pH 5.5 and 62% at pH 7.4 with little further change afterward. The nanocomposite, on the other hand, continued releasing drug gradually over the full 72 hours, reaching 63.8 ± 2.2% at pH 5.5 and 58.4 ± 1.9% at pH 7.4. This slower and more sustained release is exactly what is needed for a therapeutic nanocarrier, as it can maintain effective drug levels at the target site for a longer time.

Third, both free curcumin and the nanocomposite released more drug at the lower pH (5.5) than at pH 7.4. For the nanocomposite, this pH effect is particularly useful: at pH 5.5, the zinc-imidazolate bonds in ZIF-8 weaken under acidic conditions, causing the framework to gradually break apart and release the trapped curcumin. At the same time, chitosan swells in acidic conditions as its amine groups become positively charged, creating larger gaps in the coating layer through which drug molecules can escape more easily. At pH 7.4 (normal tissue and blood), both mechanisms are less active, meaning the nanocomposite holds onto most of its drug during circulation and preferentially releases it when it reaches the acidic tumor or infection environment.

The cumulative release of 63.8 ± 2.2% at pH 5.5 over 72 hours, compared to 58.4 ± 1.9% at pH 7.4, reflects the expected outcome of a multi-barrier, pH-responsive nanocomposite system and should not be interpreted as evidence of an incomplete or contradictory release mechanism. Several interconnected factors collectively account for why drug release is sustained and does not reach 100% within the 72 hour experimental window, and why this behavior is both scientifically anticipated and therapeutically desirable.

First, ZIF-8 degradation under mild acidic conditions (pH 5.5 acetate buffer) is a gradual, time-dependent process and not an instantaneous dissolution event. The zinc-imidazolate coordination bonds weaken progressively as proton activity increases, producing a slow, sustained release of encapsulated curcumin over many hours. Under pH 5.5 conditions, ZIF-8 is kinetically destabilized but far from fully dissolved within 72 h. Published studies on ZIF-8 and related zeolitic imidazolate framework nanocarriers consistently report cumulative drug release values in the range of 55–78% at pH 5.0–5.5 over 24–72 h observation windows, without complete framework dissolution, confirming that our observed 63.8% is fully within the expected mechanistic range for this class of materials.[11,12,42] Complete ZIF-8

Table 9 Summary of two-way ANOVA results for zone of inhibition, MIC, and MBC/MFC

Statistical parameter	ZOI (mm)	MIC (μg mL^{-1})	MBC/MFC (μg mL^{-1})
Treatment effect (*p*-value)	<0.001[a]	0.228 (NS)	0.142 (NS)
Microorganism effect (*p*-value)	0.022[a]	<0.001[a]	0.074 (NS)
Interaction effect (*p*-value)	0.692 (NS)	0.678 (NS)	0.702 (NS)
Most susceptible organism	*S. agalactiae*	*S. agalactiae*	*S. aureus*
Most resistant organism	*K. pneumoniae*	*K. pneumoniae*	*K. pneumoniae*/*E. coli*
Post-hoc Tukey key comparison	*S. agalactiae vs. K. pneumoniae* ($p = 0.037$)	Species differ markedly	No significant pairwise

[a] Significant at $p < 0.05$. NS = not significant. Two-way ANOVA with Tukey post-hoc test.

dissolution would require either prolonged incubation (>168 h), more strongly acidic conditions (pH ≤ 4.5), or the presence of competing chelating agents, none of which are present in the physiological tumor microenvironment and are therefore not appropriate comparators for *in vitro* release assessment.

Second, the chitosan outer coating constitutes an independent, rate-limiting diffusion barrier that the released curcumin must traverse before entering the bulk release medium. Even after partial ZIF-8 degradation liberates drug molecules from the MOF pore network, diffusion through the swollen but structurally intact chitosan polymer matrix imposes additional kinetic resistance. This dual-barrier (ZIF-8 + chitosan) architecture is quantitatively captured by the Korsmeyer–Peppas release exponent $n = 0.61$ at pH 5.5 (anomalous, non-Fickian transport), confirming that release is governed simultaneously by framework degradation and polymer chain relaxation rather than by simple Fickian diffusion alone. The meaningfully higher n value at pH 5.5 compared to pH 7.4 (0.61 *vs.* 0.53) demonstrates that chitosan swelling makes a larger mechanistic contribution in the acidic environment, consistent with the known pH-sensitive protonation of chitosan amine groups.[16,17]

Third, curcumin is not merely confined within ZIF-8 pores by physical trapping but is additionally retained by non-covalent host–guest interactions including π–π stacking between curcumin's extended aromatic system and the imidazolate linkers, and hydrogen bonding of the curcumin enol O–H with Zn–N coordination sites (confirmed by the FTIR bathochromic shift of the C=O/C=C conjugated band from 1626 to 1606 cm^{-1}, Section 3.2.5). These host–guest binding interactions require thermodynamic or kinetic energy to overcome, meaning that a residual fraction of curcumin remains associated with partially intact or degraded ZIF-8 fragments throughout the experimental period. Complete displacement of this bound fraction would require conditions beyond those of the physiological acidic microenvironment.

Critically, the 5.4 percentage-point differential in cumulative release between pH 5.5 (63.8%) and pH 7.4 (58.4%) confirms authentic, statistically significant pH-responsiveness ($p < 0.05$). For a targeted nanocarrier, incomplete release over 72 hours is not a formulation failure but a deliberate design outcome. A system releasing 100% of its payload rapidly at both pH values would be functionally indistinguishable from a simple burst-release formulation and would provide no preferential selectivity for the tumor/infection microenvironment over systemic circulation. The sustained, pH-dependent release profile maintained over 72 h ensures prolonged drug exposure above the MIC at the pathological site, fulfilling the primary pharmacokinetic objective of a controlled-release nanocarrier. Drug release is governed by pH-triggered progressive weakening of Zn–N coordination bonds, coupled with chitosan chain swelling, which results in anomalous non-Fickian transport and preferentially accelerated drug release in acidic microenvironments. This mechanistic interpretation is fully consistent with both the experimental release data and the kinetic modeling results.

Table 10 Comparison of antimicrobial parameters of the present nanocomposite with published data for related compounds and free curcumin

Study/compound	Organism	ZOI (mm)	MIC	MBC
Present study: Cur/Fe_3O_4@ZIF-8@CS	*S. agalactiae*	20.00 ± 2.00	11.07 ± 3.93 μg mL^{-1}	62.47 ± 54.16 μg mL^{-1}
Present study: Cur/Fe_3O_4@ZIF-8@CS	*S. aureus*	18.67 ± 3.60	18.57 ± 11.54 μg mL^{-1}	52.10 ± 18.01 μg mL^{-1}
Present study: Cur/Fe_3O_4@ZIF-8@CS	*E. coli*	14.67 ± 3.06	13.33 ± 3.92 μg mL^{-1}	104.17 ± 36.05 μg mL^{-1}
Present study: Cur/Fe_3O_4@ZIF-8@CS	*K. pneumoniae*	14.67 ± 3.06	104.17 ± 36.08 μg mL^{-1}	104.17 ± 36.08 μg mL^{-1}
El-Khawaga *et al.* 2024 ($MgFe_2O_4$ NPs, 30 μg mL^{-1})[50]	*S. aureus*	23	2.5 μg mL^{-1}	—
El-Khawaga *et al.* 2024 ($MgFe_2O_4$ NPs, 30 μg mL^{-1})[50]	*E. coli*	26	1.25 μg mL^{-1}	—
Rahvar *et al.* 2021 (Zn-BDC MOF)[51]	*S. aureus*	8	—	—
Rahvar *et al.* 2021 (Zn-BDC MOF)[51]	*E. coli*	9	—	—
Wada *et al.* 2021 (free curcumin, 100 mg mL^{-1})[58]	*S. aureus*	13	—	—
Wada *et al.* 2021 (free curcumin, 100 μg mL^{-1})[58]	*K. pneumoniae*	7	—	—
Górski *et al.* 2022 (free curcumin)[52]	*S. aureus*	—	0.046 mg mL^{-1} (mean)	0.19 mg mL^{-1} (mean)
Górski *et al.* 2022 (free curcumin)[52]	*E. coli*	—	0.885 mg mL^{-1} (mean)	3.54 mg mL^{-1} (mean)
Górski *et al.* 2022 (free curcumin)[52]	*K. pneumoniae*	—	1.04 mg mL^{-1} (mean)	>2.5 mg mL^{-1}

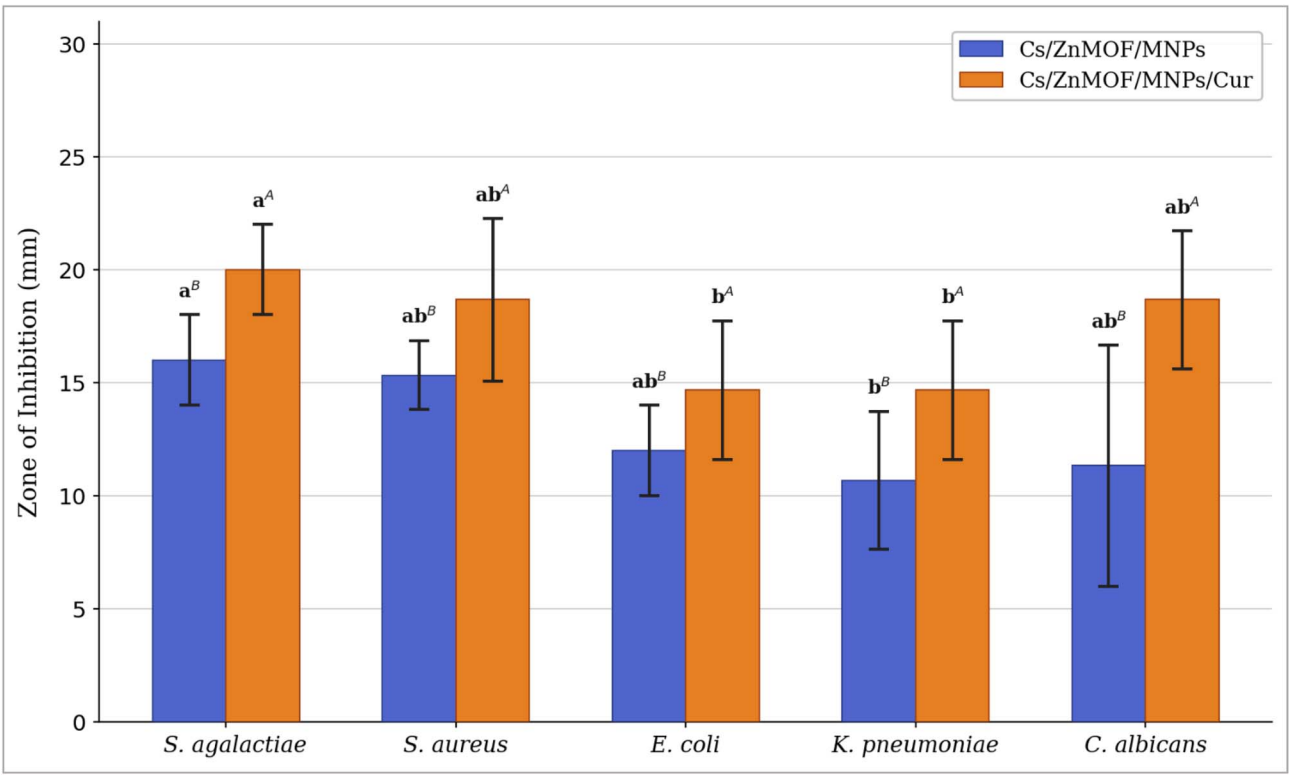

Fig. 9 Zone of inhibition (mm) of Fe_3O_4@ZIF-8@CS and Cur/Fe_3O_4@ZIF-8@CS against five clinical microbial strains. Data are presented as mean ± SD ($n = 3$). Lowercase letters (a and b) above bars indicate significant differences among microbial species within each treatment group ($p < 0.05$, two-way ANOVA with Tukey post-hoc test). Uppercase letters (A and B) indicate significant differences between the two treatments within each species ($p < 0.05$). Treatment effect: $p < 0.001$; species effect: $p = 0.022$; interaction: $p = 0.692$ (NS).

3.4 Drug release kinetics

Table 7 shows the fitting results for all four kinetic models applied to both free curcumin and the nanocomposite at both pH values.

For free curcumin, the Higuchi model gave the best fit ($R^2 =$ 0.961 at pH 5.5 and 0.937 at pH 7.4), and the Korsmeyer–Peppas exponent n was 0.38–0.41. Both of these results point to simple Fickian diffusion as the mechanism: curcumin molecules in the Tween-80 vehicle move passively from high concentration to low concentration with no physical resistance slowing them down, following a square-root-of-time pattern.

For the nanocomposite, the Korsmeyer–Peppas model gave the best fit ($R^2 = 0.994$ at pH 5.5 and 0.981 at pH 7.4), and the n values were 0.61 (pH 5.5) and 0.53 (pH 7.4). These n values fall between 0.43 and 0.85, which indicates anomalous (non-Fickian) transport—meaning that release is controlled by two things happening at the same time: drug diffusing through the MOF pore network, and the chitosan polymer layer gradually swelling and relaxing. Neither mechanism alone is fast enough to match the Higuchi or first-order models; instead, both work together to produce the sustained release profile seen in the data.

The higher n value at pH 5.5 compared to pH 7.4 (0.61 *vs.* 0.53) shows that polymer swelling plays a bigger role at lower pH, which is consistent with the known pH-sensitive behavior of chitosan. The first-order rate constants also confirm the benefit of encapsulation: curcumin releases 2.2 times more slowly from the nanocomposite than from the Tween-80 vehicle at pH 5.5, and 2.7 times more slowly at pH 7.4, providing a quantitative measure of the sustained-release advantage.

3.5 Antimicrobial activity

The antimicrobial performance of the blank nanocomposite (Fe_3O_4@ZIF-8@CS), the curcumin-loaded nanocomposite (Cur/Fe_3O_4@ZIF-8@CS), and free curcumin as a parallel experimental control was assessed against five clinical microbial strains using three standard assays: agar well diffusion (zone of inhibition, ZOI), minimum inhibitory concentration (MIC), and minimum bactericidal/fungicidal concentration (MBC/MFC). The complete results are presented in Table 8. Statistical significance was evaluated by two-way ANOVA with Tukey post-hoc test, and the key statistical outcomes are summarized in Table 9. A comparison with relevant published data for similar compounds is provided in Table 10.

3.5.1 Zone of inhibition. The agar well diffusion results showed that the curcumin-loaded nanocomposite produced consistently larger inhibition zones than the blank nanocomposite across all five tested organisms (Table 9 and Fig. 9). Two-way ANOVA confirmed that the difference between the two treatments was statistically significant ($p < 0.001$), indicating that the addition of curcumin meaningfully enhanced the antimicrobial effect of the nanocarrier system. A significant

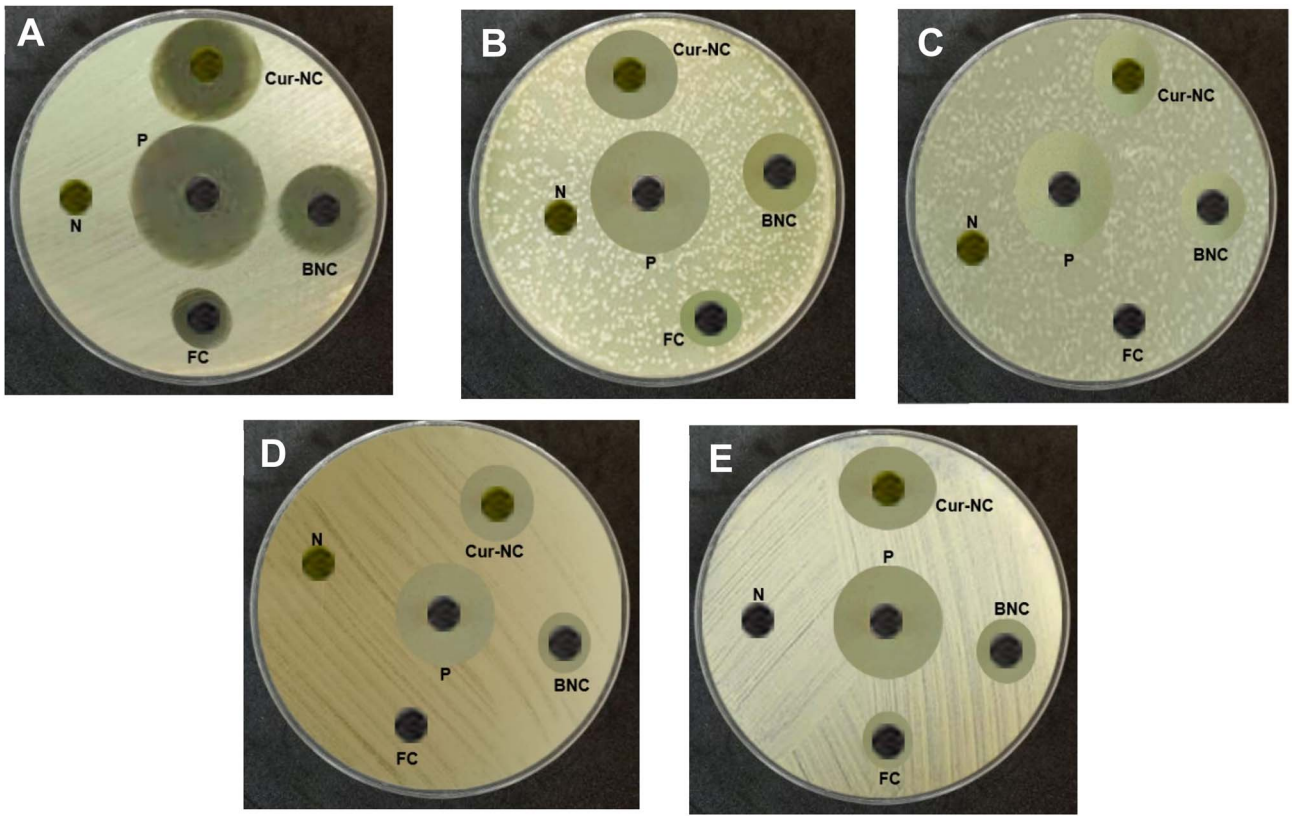

Fig. 10 Representative agar well diffusion plate photographs showing zones of inhibition (ZOI, mm) against (A) *Streptococcus agalactiae*, (B) *Staphylococcus aureus*, (C) *Escherichia coli*, (D) *Klebsiella pneumoniae*, and (E) *Candida albicans*. BNC = Fe_3O_4@ZIF-8@CS (blank nanocomposite, 1000 μg mL^{-1}); Cur-NC = Cur/Fe_3O_4@ZIF-8@CS (curcumin-loaded nanocomposite, 1000 μg mL^{-1}); FC = free curcumin (1000 μg mL^{-1} in 0.5% DMSO); P = positive control (streptomycin 10 μg mL^{-1} for bacterial strains; fluconazole 25 μg mL^{-1} for *C. albicans*); N = negative control (0.5% DMSO vehicle).

effect of microbial species was also detected ($p = 0.022$). No significant interaction between treatment type and microbial species was found ($p = 0.692$).

Among all tested organisms, *S. agalactiae* was the most susceptible. The blank nanocomposite produced a ZOI of 16.00 ± 2.00 mm, and this increased significantly to 20.00 ± 2.00 mm with curcumin loading ($p < 0.05$). *K. pneumoniae* showed the smallest ZOI values: 10.67 ± 3.06 mm (blank) and 14.67 ± 3.06 mm (curcumin-loaded). *S. aureus* showed ZOI values of 15.33 ± 1.53 mm (blank) and 18.67 ± 3.60 mm (curcumin-loaded). A notable result was obtained for *C. albicans*: the blank nanocomposite produced a ZOI of only 11.33 ± 5.33 mm, while the curcumin-loaded system more than doubled this to 18.67 ± 3.06 mm.

The addition of free curcumin as a parallel experimental control group provides direct, within-experiment quantitative evidence for the antimicrobial advantage of nanoencapsulation. Free curcumin at 1000 μg mL^{-1} produced no detectable inhibition zone against *E. coli* or *K. pneumoniae*, and only modest ZOI values of 8.33 ± 1.53 mm (*S. agalactiae*), 7.67 ± 1.15 mm (*S. aureus*), and 6.67 ± 2.08 mm (*C. albicans*). By contrast, the curcumin-loaded nanocomposite at the same total curcumin-equivalent concentration produced ZOI values of 20.00 ± 2.00, 18.67 ± 3.60, 14.67 ± 3.06, 14.67 ± 3.06, and 18.67 ± 3.06 mm for the five respective organisms. This represents a 1.5- to >2-fold amplification in ZOI relative to free curcumin, and the complete absence of activity for free curcumin against the two Gram-negative organisms *versus* measurable inhibition by both nanocomposite formulations confirms that the nanocarrier platform, not curcumin solubility alone, is responsible for the observed potency. These within-experiment results are consistent with the MIC advantage quantified below and with published free curcumin data.[50,51]

The general trend of lower ZOI values for the two Gram-negative organisms compared to the Gram-positive ones is consistent with the known structural differences between these bacterial groups. Gram-negative bacteria possess an outer membrane that acts as an additional physical barrier, limiting the penetration of many antimicrobial agents into the cell.[50] The fact that both nanocomposite formulations still produced measurable inhibition against these organisms reflects the ability of nanoparticles to interact with and disrupt this outer membrane through physical contact and ion release.

To provide direct visual evidence of the inhibitory activity observed across all five tested organisms, representative agar well diffusion plate photographs are presented in Fig. 10. The images show clearly delineated zones of inhibition for Fe_3O_4@ZIF-8@CS, Cur/Fe_3O_4@ZIF-8@CS, and the positive

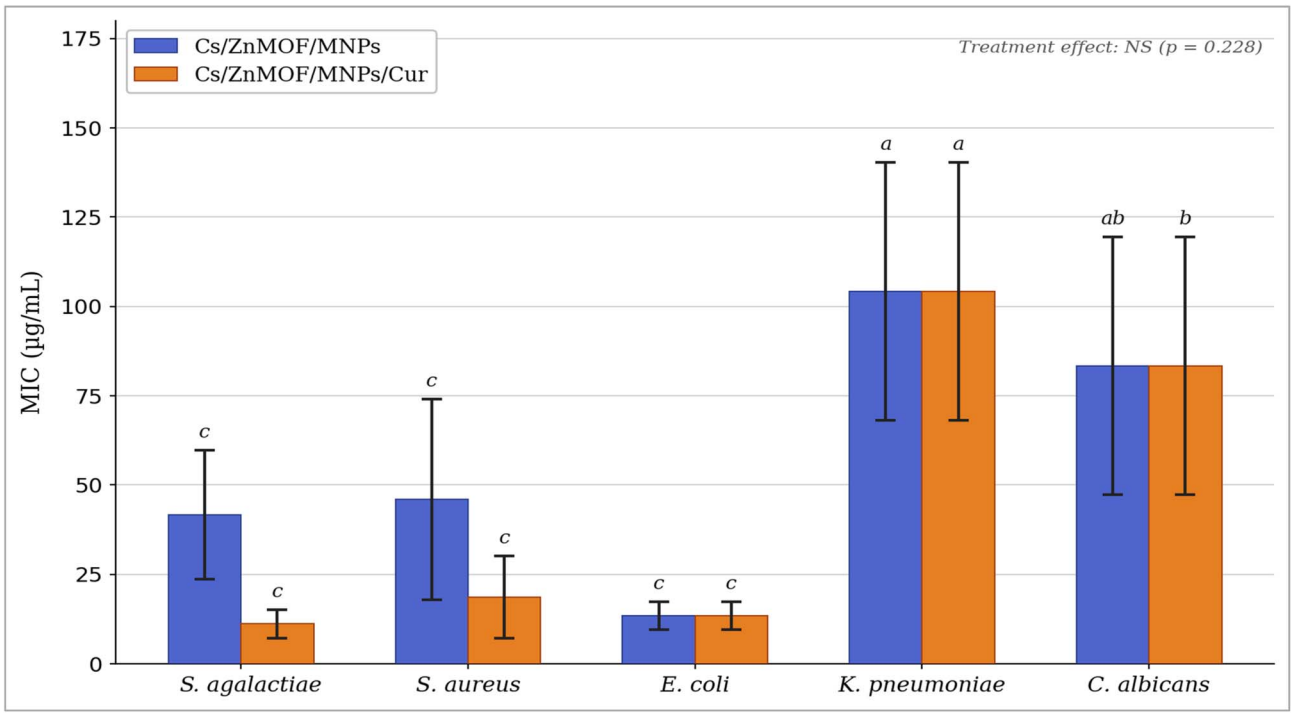

Fig. 11 Minimum inhibitory concentration (MIC, μg mL^{-1}) of Fe_3O_4@ZIF-8@CS and Cur/Fe_3O_4@ZIF-8@CS against five clinical microbial strains. Data are presented as mean ± SD ($n = 3$). Lowercase letters (a–c) above bars indicate significant differences among microbial species ($p < 0.05$, two-way ANOVA with Tukey post-hoc test). No significant difference between the two treatments was detected ($p = 0.228$, NS). Interaction effect: $p = 0.678$ (NS).

controls after 24 h incubation at 37 °C, with ZOI diameters annotated directly on the photographs. The complete absence of any measurable inhibition zone for the 0.5% DMSO vehicle control confirms that the observed antimicrobial effects are attributable solely to the test formulations and not to the solvent. The photographic ZOI measurements are in full quantitative agreement with the mean ± SD values reported in Table 8.

3.5.2 Minimum inhibitory concentration (MIC). Two-way ANOVA of the MIC data showed no statistically significant main effect of treatment type ($p = 0.228$), meaning that at the concentrations tested, the blank and curcumin-loaded nanocomposites did not differ significantly in their ability to inhibit growth, Table 9. However, microbial species had a highly significant effect on MIC values ($p < 0.001$), reflecting large differences in natural susceptibility between the five organisms. No significant interaction between treatment and species was found ($p = 0.678$), confirming that the two formulations behaved similarly across all organisms without any species-specific advantage.

S. agalactiae was the most sensitive organism to the curcumin-loaded nanocomposite, with an MIC of 11.07 ± 3.93 μg mL^{-1}. This was the lowest MIC value recorded across the entire study and was significantly lower than the MIC for *K. pneumoniae* ($p < 0.001$, lowercase superscripts c *vs.* a). The blank nanocomposite required a considerably higher concentration of 41.70 ± 18.01 μg mL^{-1} to inhibit *S. agalactiae*, representing a roughly 3.8-fold reduction in the inhibitory concentration with curcumin loading.

S. aureus also showed a meaningful improvement in MIC with curcumin loading: from 46.00 ± 28.06 μg mL^{-1} (blank) to 18.57 ± 11.54 μg mL^{-1} (curcumin-loaded), a 2.5-fold reduction. This is clinically relevant given the importance of *S. aureus* as a leading cause of wound infections and hospital-acquired infections. Both MIC values fall in the range of low superscript c, sharing the same statistical grouping with *S. agalactiae* and *E. coli*, indicating these three organisms were significantly more susceptible than *K. pneumoniae* and *C. albicans*.

E. coli showed equal MIC values for both formulations: 13.33 ± 3.93 μg mL^{-1} (blank) and 13.33 ± 3.92 μg mL^{-1} (curcumin-loaded). This indicates that for this organism, the blank nanocomposite was already sufficient to inhibit growth at this concentration and curcumin addition did not lower the inhibitory threshold further. In contrast, *K. pneumoniae* was the most resistant organism, with MIC values of 104.17 ± 36.08 μg mL^{-1} for both formulations. *K. pneumoniae* is intrinsically resistant to many antimicrobials due to its efficient outer membrane barrier and the frequent presence of beta-lactamase enzymes in clinical isolates, and this is reflected in the high MIC values observed here. *C. albicans* required 83.33 ± 36.08 μg mL^{-1} to inhibit growth for both treatments, confirming moderate susceptibility of this fungal species, as shown in Fig. 11.

Direct experimental comparison with the free curcumin control group reveals a dramatic advantage of nanoencapsulation. Free curcumin required >500 μg mL^{-1} for

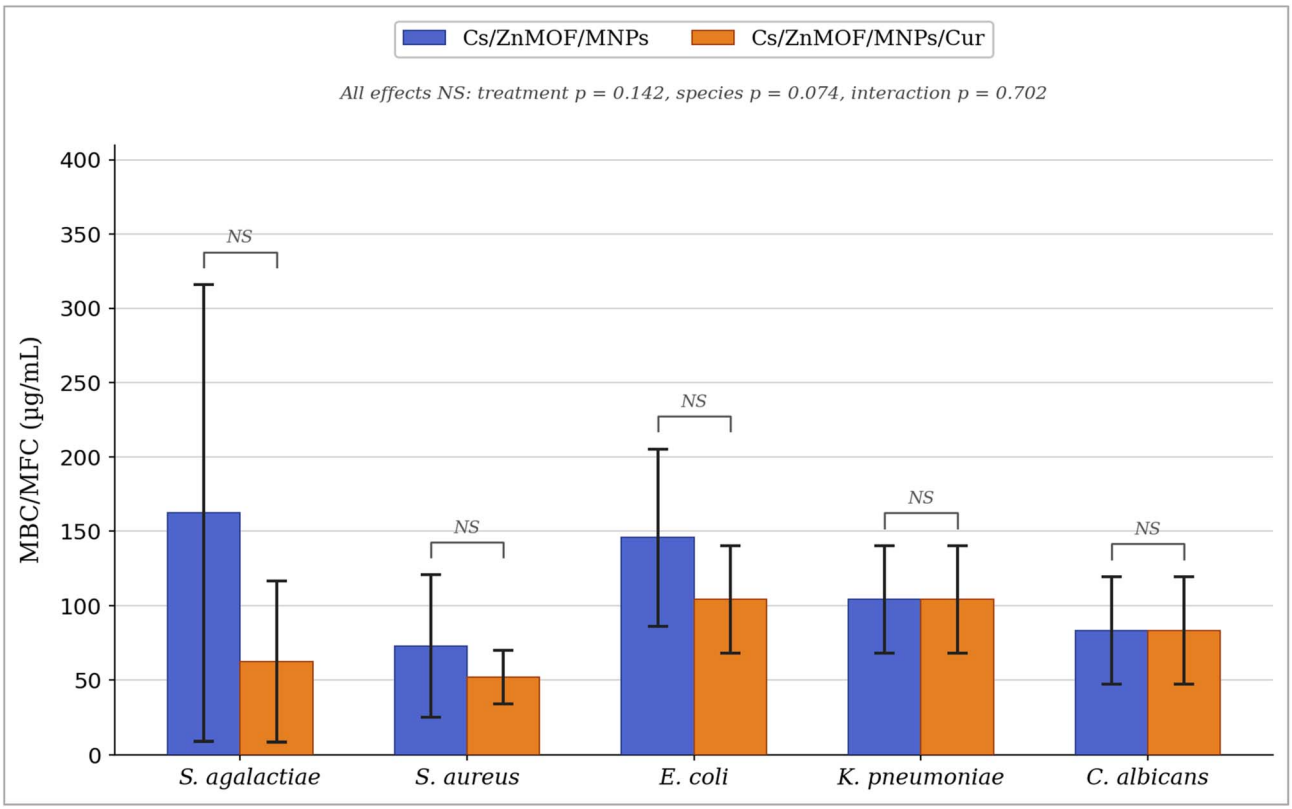

Fig. 12 Minimum bactericidal/fungicidal concentration (MBC/MFC, μg mL^{-1}) of Fe_3O_4@ZIF-8@CS and Cur/Fe_3O_4@ZIF-8@CS against five clinical microbial strains. Data are presented as mean ± SD ($n = 3$). NS brackets above each species pair indicate no significant difference between treatments ($p > 0.05$). No statistically significant effects were detected for treatment ($p = 0.142$), microbial species ($p = 0.074$), or their interaction ($p = 0.702$). Two-way ANOVA with Tukey post-hoc test.

inhibition of Gram-positive organisms and exceeded >1000 μg mL^{-1} for both Gram-negative species and *C. albicans*. The corresponding MIC reductions achieved by Cur/Fe_3O_4@ZIF-8@CS relative to free curcumin are: >45-fold for *S. agalactiae* (11.07 *vs.* >500 μg mL^{-1}), >27-fold for *S. aureus* (18.57 *vs.* >500 μg mL^{-1}), >75-fold for *E. coli* (13.33 *vs.* >1000 μg mL^{-1}), and >10-fold for *K. pneumoniae* (104.17 *vs.* >1000 μg mL^{-1}). These within-experiment MIC reductions directly validate that the Cur/Fe_3O_4@ZIF-8@CS nanoplatform overcomes the inherent bioavailability and aqueous solubility limitations of free curcumin through encapsulation-mediated delivery, concentration at the bacterial cell surface, and protection from premature chemical degradation in the assay medium.

When these MIC values are compared against published data for the individual components used in isolation, the advantage of the nanocomposite approach becomes apparent. Górski *et al.* (2022) reported that free curcumin showed a mean MIC of 0.885 mg mL^{-1} (885 μg mL^{-1}) against *E. coli* which is approximately 66 times higher than the MIC of the curcumin-loaded nanocomposite (13.33 μg mL^{-1}) found in the present study.[52] Against *S. aureus*, Górski *et al.* reported a mean free curcumin MIC of 0.046 mg mL^{-1} (46 μg mL^{-1}), compared to 18.57 μg mL^{-1} for Cur/Fe_3O_4@ZIF-8@CS showing a 2.5-fold improvement. For *K. pneumoniae*, free curcumin MIC was reported as 1.04 mg mL^{-1} (1040 μg mL^{-1}), compared to 104.17 μg mL^{-1} here is a 10-fold reduction. These improvements confirm that nanoencapsulation substantially enhances the delivery and effectiveness of curcumin, even against the more resistant organisms.

3.5.3 Minimum bactericidal and fungicidal concentration (MBC/MFC). The MBC/MFC results showed no statistically significant main effect of treatment type ($p = 0.142$), no significant main effect of microbial species ($p = 0.074$), and no significant interaction between the two factors ($p = 0.702$), as shown in Fig. 12 and Table 9. These findings indicate that both the blank and curcumin-loaded nanocomposites have broadly comparable bactericidal and fungicidal activity at the concentrations tested, and that this killing activity is generally consistent across the tested organisms without marked species-specific differences.

The lowest MBC values were found for *S. aureus*: 72.93 ± 47.71 μg mL^{-1} (blank nanocomposite) and 52.10 ± 18.01 μg mL^{-1} (curcumin-loaded). The reduction in MBC with curcumin loading reflects the additional intracellular killing action of curcumin once it is internalized by bacteria that have already been weakened by the nanoparticle framework and chitosan components. *S. agalactiae* showed the largest absolute reduction in MBC between the two formulations: from 162.53 ± 153.48 μg mL^{-1} (blank) to 62.47 ± 54.16 μg mL^{-1} (curcumin-loaded), a 2.6-fold improvement, although the wide standard

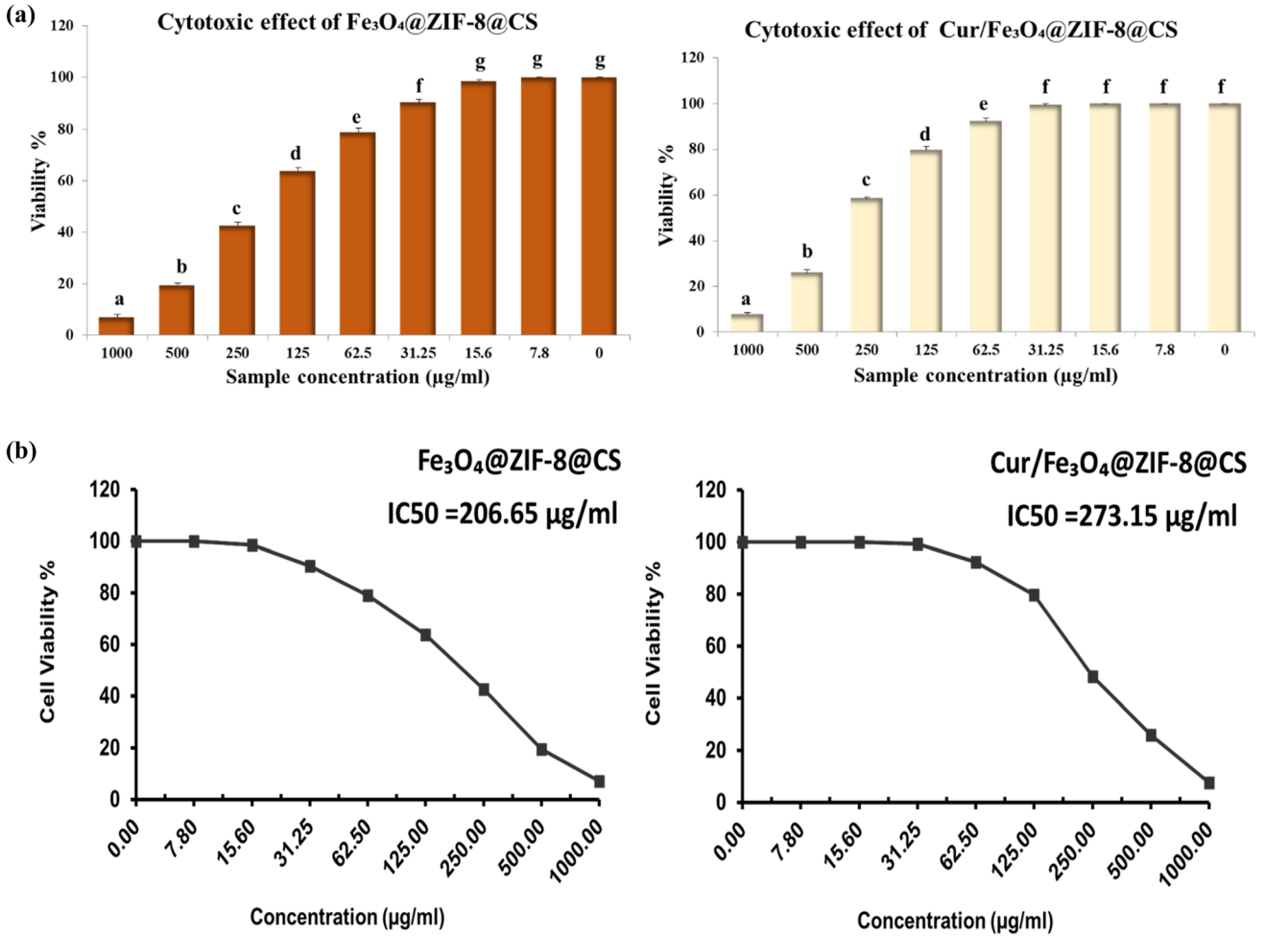

Fig. 13 (a) Cytotoxic effect of Fe_3O_4@ZIF-8@CS and Cur/Fe_3O_4@ZIF-8@ CS against L929 cell line at various concentrations. (b) IC_{50} values of Fe_3O_4@ZIF-8@CS and Cur/Fe_3O_4@ZIF-8@ CS against L929 cell line.

deviations suggest variability between replicates for this organism.

E. coli required higher concentrations for bactericidal activity: 145.83 ± 59.47 µg mL^{-1} (blank) and 104.17 ± 36.05 µg mL^{-1} (curcumin-loaded), while *K. pneumoniae* showed equal MBC and MIC values of 104.17 ± 36.08 µg mL^{-1} for both formulations. When MBC equals MIC, the compound acts as a bactericide rather than a bacteriostat at the inhibitory concentration; meaning that the concentration required to stop growth is also sufficient to kill the bacteria. This bactericidal mode of action at the MIC is pharmacologically favourable, particularly for infections in immunocompromised patients, where bacteriostatic drugs alone may be insufficient to achieve clinical cure.[53] *C. albicans* also showed equal MIC and MFC values of 83.33 ± 36.08 µg mL^{-1} for both formulations, confirming fungicidal activity at the inhibitory concentration.

Comparing the MBC values with published free curcumin data again demonstrates the nanocomposite advantage. Górski *et al.* (2022)[52] reported a mean MBC of 3.54 mg mL^{-1} (3540 µg mL^{-1}) for free curcumin against *E. coli*, compared to 104.17 µg mL^{-1} achieved here with Cur/Fe_3O_4@ZIF-8@CS that is a roughly 34-fold reduction in the concentration needed to kill the bacteria. Against *S. aureus*, Górski *et al.* found a mean MBC of 0.19 mg mL^{-1} (190 µg mL^{-1}) for free curcumin, compared to 52.10 µg mL^{-1} in the present study which is a 3.6-fold improvement. These comparisons confirm that the nanocomposite system substantially reduces the bactericidal dose compared to free curcumin.

3.5.4 Mechanisms of antimicrobial action. The superior antimicrobial activity of Cur/Fe_3O_4@ZIF-8@CS compared to the blank nanocomposite, and both compared to free curcumin reported in the literature, can be explained by the combined and cooperative action of all four components in the nanocomposite system, Table 10. The magnitude of the observed improvements is further contextualized by direct comparison with published data for the individual components in isolation (Table 10); the nanocomposite consistently outperforms both free curcumin and single-component nanoparticle systems across all tested organisms, confirming the synergistic, multi-mechanism advantage of the integrated Fe_3O_4@ZIF-8@CS architecture.

Table 11 Physicochemical stability of the optimized Cur/Fe_3O_4@ZIF-8@CS nanocomposite stored at 25 ± 2 °C and under accelerated conditions (40 ± 2 °C/75 ± 5% RH, ICH Q1A(R2)) at T_0, T_1 (1 month), and T_2 (2 months) (n = 3, mean ± SD)

		Time point		
Parameter	Storage condition	T_0 (day 0)	T_1 (1 month)	T_2 (2 months)
Particle size (nm)	25 ± 2 °C	228.6 ± 4.7	234.2 ± 5.1	241.8 ± 5.8
	40 ± 2 °C/75 ± 5% RH	228.6 ± 4.7	248.7 ± 6.2	263.5 ± 7.4
PDI	25 ± 2 °C	0.218 ± 0.010	0.224 ± 0.011	0.231 ± 0.012
	40 ± 2 °C/75 ± 5% RH	0.218 ± 0.010	0.241 ± 0.013	0.258 ± 0.015
Zeta potential (mV)	25 ± 2 °C	+31.5 ± 1.4	+30.1 ± 1.2	+28.7 ± 1.5
	40 ± 2 °C/75 ± 5% RH	+31.5 ± 1.4	+27.3 ± 1.6	+24.9 ± 1.8
Curcumin retention (%)	25 ± 2 °C	100.0 ± 0.0	97.4 ± 1.2	94.6 ± 1.8
	40 ± 2 °C/75 ± 5% RH	100.0 ± 0.0	92.8 ± 2.1	87.9 ± 2.6

Fe_3O_4 magnetic nanoparticles contribute to antimicrobial activity through three main mechanisms. First, the nanoparticles make direct physical contact with bacterial cell membranes and disrupt their structural integrity, causing leakage of cellular contents. Second, iron ions released from the nanoparticle surface interfere with bacterial metalloenzymes and disrupt key metabolic pathways. Third, Fe_3O_4 nanoparticles catalyze the generation of reactive oxygen species (ROS) including hydroxyl radicals and superoxide through Fenton-like reactions, which causes oxidative damage to bacterial DNA, membrane lipids, and proteins simultaneously.[54] Additionally, Fe_3O_4 nanoparticles are inexpensive and have low toxicity toward mammalian cells, which makes them suitable for incorporation into therapeutic formulations.[55]

Chitosan, which forms the outer coating layer of the nanocomposite, contributes to antimicrobial activity mainly through its positive surface charge. At physiological pH, the protonated amine groups ($-NH_3^+$) of chitosan bind strongly to the negatively charged components of bacterial and fungal cell walls including phospholipids, lipopolysaccharides (in Gram-negative bacteria), and peptidoglycans (in Gram-positive bacteria) through electrostatic attraction. This interaction disrupts membrane permeability and causes cell lysis. Beyond its direct antimicrobial action, chitosan serves as a stabilizing matrix that prevents the Fe_3O_4 nanoparticles from aggregating and maintains the nanocomposite as a stable, well-dispersed suspension, ensuring consistent and reproducible contact with microbial cells.[17,18]

The zinc-based MOF (ZnMOF) framework contributes to antimicrobial activity primarily through the release of Zn^{2+} ions as the framework gradually degrades under physiological conditions. Zinc ions are well-documented antimicrobials: they inhibit the active sites of key bacterial enzymes, block transport proteins in the cell membrane, interfere with DNA replication, and increase membrane permeability. The carboxylate (COO^-) and amine groups on the MOF organic linkers also interact directly with bacterial cell surfaces, contributing additional disruption to cell wall integrity and promoting ROS generation by zinc-mediated redox activity.[56]

Curcumin, as the active pharmaceutical ingredient loaded within the MOF pores, adds its own well-studied antimicrobial mechanisms to these framework effects. Inside the microbial cell, curcumin disrupts DNA replication by intercalating into double-stranded DNA, alters gene expression by modulating transcription factor activity, and damages the cell membrane by interacting with membrane phospholipids and increasing membrane fluidity. Curcumin also generates intracellular ROS, amplifying the oxidative stress already initiated by the Fe_3O_4 component.[57] The key advantage of nanoencapsulation within the ZIF-8 pores is that curcumin is protected from chemical degradation and is released in a controlled manner directly at the site of microbial contact, rather than degrading in the surrounding medium before it can reach the bacterial cell which is the main reason why free curcumin requires concentrations orders of magnitude higher to achieve equivalent effects.

Taken together, the results of this study demonstrate that Cur/Fe_3O_4@ZIF-8@CS is a multifunctional antimicrobial system in which all four components including chitosan, the zinc MOF, Fe_3O_4 magnetic nanoparticles, and curcumin work together through complementary and synergistic mechanisms. The nanocomposite is effective against both Gram-positive and Gram-negative bacteria as well as the fungal pathogen *C. albicans*, and it achieves this activity at concentrations that are dramatically lower than those required by any individual component alone, as illustrated in Table 10.

3.6 Concentration-dependent cytotoxicity and IC_{50} determination in mouse fibroblast cells

A concentration dependent cytotoxic effect was recorded on exposure the mouse fibroblast cell line to the Fe_3O_4@ZIF-8@CS and Cur/Fe_3O_4@ZIF-8@CS as illustrated in Fig. 13a. Whereas the viability% of the cells decreased with increasing the concentration, the lowest viability% (7.10% and 7.67%) for Fe_3O_4@ZIF-8@CS and Cur/Fe_3O_4@ZIF-8@CS respectively was reported at 1000 μg mL^{-1}. This result is similar to the results obtained by Tamames-Tabar *et al.* (2014)[59] and Ettlinger *et al.*, (2020).[41] The cytotoxic effect at higher concentration may be resulted from the triggered autophagic effect by ZIF-8, that enhance its degradation and subsequently Zn^{2+} leakages that enhances autophagy and induces generation of ROS.[60]

Additionally, the IC_{50} value of Fe_3O_4@ZIF-8@CS reached bout (206.65 μg mL^{-1}) and (273.15 μg mL^{-1}) for Cur/Fe_3O_4@-ZIF-8@ CS, indicating the higher cytotoxic effect of Fe_3O_4@ZIF-

8@CS than Cur/Fe_3O_4@ZIF-8@ CS Fig. 13b. This may be attributed to the suitable size of the Cur/Fe_3O_4@ZIF-8@ CS that increasing their passage through the cell membrane; moreover, the PH-responsiveness of ZIF-8 may elevate the local concentration of curcumin.[61] It is reported that ZIF-8 has the ability to improve the rate of drug release within an acidic environment and enhancing drug delivery systems.[42]

3.7 Stability study

The physicochemical stability of the optimized Cur/Fe_3O_4@ZIF-8@CS nanocomposite was systematically monitored over two months under both long-term (25 ± 2 °C) and accelerated (40 ± 2 °C/75 ± 5% RH, ICH Q1A(R2)) storage conditions. Four critical quality attributes were tracked at T_0, T_1 (1 month), and T_2 (2 months): hydrodynamic particle size, PDI, zeta potential, and curcumin content retention. The complete dataset is summarized in Table 11.

3.7.1 Particle size and PDI. At T_0, the hydrodynamic diameter was 228.6 ± 4.7 nm. During long-term storage, the size increased slightly to 241.8 ± 5.8 nm at T_2, remaining within the EPR-targeting range of 100–400 nm.[62] Under accelerated conditions, the size increased to 263.5 ± 7.4 nm, but still satisfied the therapeutic size criterion. The increase is attributed to chitosan swelling, surface hydration, and minor Ostwald ripening of the ZIF-8 shell, which are commonly observed for polymer-coated nanoparticles at elevated temperature and humidity.[63,64] The relatively small change compared with chitosan-coated liposomal systems reported by Liu *et al.*[63] suggests that the rigid ZIF-8 framework improves structural stability. Similar temperature-induced particle growth has also been reported by Zheng *et al.*[64] and Winarti and Sunarti.[65]

PDI followed the same trend, increasing from 0.218 ± 0.010 at T_0 to 0.231 ± 0.012 (25 °C) and 0.258 ± 0.015 (40 °C/75% RH) at T_2. All values remained below the homogeneity limit of 0.30,[66] confirming that the nanocomposite maintained a narrow size distribution during storage, consistent with previous reports for chitosan-coated systems.[63]

3.7.2 Zeta potential. The initial zeta potential was +31.5 ± 1.4 mV, exceeding the ±20 mV stability threshold.[66] During long-term storage, it decreased slightly to +28.7 ± 1.5 mV, while accelerated storage caused a reduction to +24.9 ± 1.8 mV. However, values remained above +20 mV, indicating maintained colloidal stability.

The decrease is likely due to partial deprotonation of chitosan amine groups, amine hydrolysis, and ionic screening caused by moisture uptake.[31,66] Similar behavior was reported for chitosan-coated curcumin liposomes under thermal stress.[63] Importantly, the positive charge remained above +24 mV, suggesting sufficient electrostatic repulsion and preserved antimicrobial interaction with bacterial membranes.[63]

3.7.3 Curcumin content retention. Curcumin content was determined at 425 nm and expressed as retention (%) = $C_t/C_0 \times 100$. At 25 ± 2 °C, retention remained high (97.4 ± 1.2% at T_1 and 94.6 ± 1.8% at T_2), corresponding to only 5.4% loss over two months. Under accelerated conditions, retention decreased to 92.8 ± 2.1% at T_1 and 87.9 ± 2.6% at T_2, but remained above the ≥80% pharmaceutical acceptability threshold.[67]

The improved stability is attributed to encapsulation within the ZIF-8 pores and protection by the chitosan shell, which limits oxidation and moisture diffusion.[31,63] Liu *et al.*[63] reported 75.77% retention for chitosan-coated liposomal curcumin after 40 days, which is lower than the 94.6% observed here after 60 days, indicating stronger protection by the MOF structure. Faster degradation at elevated temperature agrees with previous reports for encapsulated curcumin systems,[64,65] and is mainly related to thermally induced β-diketone cleavage and partial framework destabilization.[31,32]

3.7.4 Physical appearance. Samples stored at 25 ± 2 °C showed no visible aggregation, sedimentation, or color change up to T_2, confirming good colloidal stability. Under accelerated conditions, slight fading of the characteristic yellow color was observed at T_2, consistent with the measured reduction in curcumin content. Similar temperature-dependent color loss has been reported for curcumin-loaded systems, where discoloration correlated with curcumin degradation.[64,65]

3.7.5 Overall stability assessment. All evaluated parameters remained within acceptable pharmaceutical limits over two months under both storage conditions. Temperature was the main factor affecting stability, with slightly larger changes observed under accelerated conditions (40 ± 2 °C/75 ± 5% RH, ICH Q1A(R2)[68]). Overall, the ZIF-8/chitosan architecture provided strong protection for curcumin compared with free drug[31,32] and previously reported chitosan-coated liposomal systems,[63] supporting the stability of Cur/Fe_3O_4@ZIF-8@CS for further pharmaceutical development.

4 Conclusion

This study demonstrated the successful rational design of a multifunctional curcumin-loaded magnetic MOF–chitosan nanocomposite (Cur/Fe_3O_4@ZIF-8@CS) as an advanced drug delivery platform. The integration of a QbD-driven Box–Behnken optimization strategy enabled a systematic and reproducible formulation process, ensuring that the optimized nanocomposite met all predefined CQAs without reliance on trial-and-error experimentation. The hierarchical assembly of Fe_3O_4, ZIF-8, and chitosan produced a structurally integrated system in which each component contributed complementary functionality: magnetic responsiveness, high drug-loading capacity, colloidal stability, and intrinsic antimicrobial properties, as comprehensively confirmed by DLS, ATR-FTIR, TEM, and VSM characterization.

The developed nanocomposite exhibited controlled, pH-responsive drug release behavior with sustained kinetics over 72 hours, indicating its suitability for preferential drug delivery in acidic pathological microenvironments such as tumors and infection sites. Nanoencapsulation dramatically enhanced the therapeutic potential of curcumin, reducing effective MIC values by up to 66-fold relative to free curcumin and producing broad-spectrum antimicrobial activity against both Gram-positive and Gram-negative bacteria as well as the fungal pathogen *Candida albicans*. A two-month ICH Q1A(R2)-guided

stability study confirmed that the ZIF-8/chitosan architecture provides robust physicochemical protection for the encapsulated drug under both long-term and accelerated storage conditions, with all quality attributes remaining within pharmaceutical acceptability limits.

Cytotoxicity evaluation by MTT assay on L929 mouse fibroblast cells confirmed a concentration-dependent effect, with IC_{50} values of 206.65 μg mL^{-1} for Fe_3O_4@ZIF-8@CS and 273.15 μg mL^{-1} for Cur/Fe_3O_4@ZIF-8@CS; the higher IC_{50} of the curcumin-loaded formulation indicates lower cytotoxicity toward normal cells, supporting an acceptable safety profile at therapeutic concentrations.

The present characterization suite encompassing DLS, ATR-FTIR, TEM, VSM, *in vitro* release, antimicrobial profiling, cytotoxicity, and two-month stability assessment constitutes a comprehensive multi-technique evaluation consistent with leading publications in the magnetic MOF nanocarrier field. Future work should incorporate X-ray photoelectron spectroscopy (XPS) to elucidate surface chemical states, and nitrogen adsorption–desorption isotherms (BET analysis) to quantify specific surface area and pore size distribution of the ZIF-8 shell before and after drug loading; these measurements would provide deeper mechanistic insight into host–guest encapsulation efficiency and guide further rational optimization. Additionally, *in vivo* pharmacokinetic studies, biocompatibility assessment under physiological conditions, and evaluation of magnetic field-guided targeting in tumor models are warranted to support translational development of this platform toward clinical applications.

Ethical statement

Not applicable, as the study did not apply to human or animal studies. The article does not include any studies on human participants or animals conducted by any of the authors.

Consent for publication

The authors confirm: this work represents original research that has not been previously published in any form. This manuscript has not been submitted for review or publication consideration elsewhere. The publication has received approval from all co-authors.

Author contributions

Donia Hemida: conceptualization, methodology, investigation, data curation, writing – original draft; Nabila Shehata: methodology, validation, formal analysis, writing – review & editing; Nada Adel El-Gaddawy: investigation, resources, data curation; Haifa E. Alfassam: formal analysis, visualization, writing – review & editing; Samar M. Mahgoub: supervision, methodology, writing – review & editing; Rehab Mahmoud: conceptualization, supervision, project administration, writing – review & editing.

Conflicts of interest

The authors declare no conflicts of interest.

Data availability

The datasets generated and/or analyzed during this study are available from the corresponding author upon reasonable request.

Acknowledgements

The authors acknowledge Princess Nourah bint Abdulrahman University Researchers Supporting Project number (PNURSP2026R400), Princess Nourah Bint Abdulrahman University, Riyadh, Saudi Arabia.

References

1 M. Naghavi, S. E. Vollset, K. S. Ikuta, L. R. Swetschinski, A. P. Gray, E. E. Wool, G. R. Aguilar, T. Mestrovic, G. Smith and C. Han, Global burden of bacterial antimicrobial resistance 1990–2021: a systematic analysis with forecasts to 2050, *Lancet*, 2024, **404**, 1199–1226.
2 C. J. L. Murray, K. S. Ikuta, F. Sharara, L. Swetschinski, G. R. Aguilar, A. Gray, C. Han, C. Bisignano, P. Rao and E. Wool, Global burden of bacterial antimicrobial resistance in 2019: a systematic analysis, *Lancet*, 2022, **399**, 629–655.
3 R. Ranjbar and M. Alam, Antimicrobial Resistance Collaborators (2022). Global burden of bacterial antimicrobial resistance in 2019: a systematic analysis, *Lancet*, 2022, **399**(10325), 629–655.
4 F. Bray, M. Laversanne, H. Sung, J. Ferlay, R. L. Siegel, I. Soerjomataram and A. Jemal, Global cancer statistics 2022: GLOBOCAN estimates of incidence and mortality worldwide for 36 cancers in 185 countries, *Ca-Cancer J. Clin.*, 2024, **74**, 229–263, DOI: 10.3322/caac.21834.
5 D. Avinash, B. Mrudula, W. Milind, N. Vanashri and S. Ravindranath, A review on nanocomposite drug delivery, *J. Drug Delivery Ther.*, 2019, **9**, 529–536.
6 Y. Yao, Y. Zhou, L. Liu, Y. Xu, Q. Chen, Y. Wang, S. Wu, Y. Deng, J. Zhang and A. Shao, Nanoparticle-based drug delivery in cancer therapy and its role in overcoming drug resistance, *Front. Mol. Biosci.*, 2020, **7**, 193.
7 J. Nel, K. Elkhoury, É. Velot, A. Bianchi, S. Acherar, G. Francius, A. Tamayol, S. Grandemange and E. Arab-Tehrany, Functionalized liposomes for targeted breast cancer drug delivery, *Bioact. Mater.*, 2023, **24**, 401–437.
8 P. Horcajada, R. Gref, T. Baati, P. K. Allan, G. Maurin, P. Couvreur, G. Férey, R. E. Morris and C. Serre, Metal–organic frameworks in biomedicine, *Chem. Rev.*, 2012, **112**, 1232–1268.
9 I. A. Lazaro and R. S. Forgan, Application of zirconium MOFs in drug delivery and biomedicine, *Coord. Chem. Rev.*, 2019, **380**, 230–259.

10 Y. Hou, C. Zhu, G. Ban, Z. Shen, Y. Liang, K. Chen, C. Wang and H. Shi, Advancements and challenges in the application of metal-organic framework (MOF) nanocomposites for tumor diagnosis and treatment, *Int. J. Nanomed.*, 2024, 6295–6317.
11 Z. Li, Y. Shao, Y. Yang and J. Zan, Zeolitic imidazolate framework-8: a versatile nanoplatform for tissue regeneration, *Front. Bioeng. Biotechnol.*, 2024, **12**, 1386534.
12 H. N. Abdelhamid, Zeolitic imidazolate frameworks (ZIF-8) for biomedical applications: a review, *Curr. Med. Chem.*, 2021, **28**, 7023–7075.
13 T. Vangijzegem, V. Lecomte, I. Ternad, L. Van Leuven, R. N. Muller, D. Stanicki and S. Laurent, Superparamagnetic iron oxide nanoparticles (SPION): from fundamentals to state-of-the-art innovative applications for cancer therapy, *Pharmaceutics*, 2023, **15**, 236.
14 Q. T. H. Shubhra, Iron oxide nanoparticles in magnetic drug targeting and ferroptosis-based cancer therapy, *Medical Review*, 2023, **3**, 444–447.
15 E. Otieno, Y. Huang, N. Li, T. Li, M. Wang, X. Qiu and X. Xiao, Utilization of superparamagnetic iron oxide nanoparticles (SPIONs) as a vector for drug delivery, *Appl. Nanosci.*, 2023, **13**, 6191–6216.
16 Y. Herdiana, N. Wathoni, S. Shamsuddin and M. Muchtaridi, Drug release study of the chitosan-based nanoparticles, *Heliyon*, 2022, **8**(1), e08674.
17 K. Jafernik, A. Ładniak, E. Blicharska, K. Czarnek, H. Ekiert, A. E. Wiącek and A. Szopa, Chitosan-based nanoparticles as effective drug delivery systems—a review, *Molecules*, 2023, **28**, 1963.
18 M. Wang, Y. Wang, G. Chen, H. Gao and Q. Peng, Chitosan-based multifunctional biomaterials as active agents or delivery systems for antibacterial therapy, *Bioengineering*, 2024, **11**, 1278.
19 E. Akdaşçi, H. Duman, F. Eker, M. Bechelany and S. Karav, Chitosan and its nanoparticles: A multifaceted approach to antibacterial applications, *Nanomaterials*, 2025, **15**, 126.
20 K. M. Nelson, J. L. Dahlin, J. Bisson, J. Graham, G. F. Pauli and M. A. Walters, The essential medicinal chemistry of curcumin: miniperspective, *J. Med. Chem.*, 2017, **60**, 1620–1637.
21 J. Yakubu and A. V Pandey, Innovative delivery systems for curcumin: Exploring nanosized and conventional formulations, *Pharmaceutics*, 2024, **16**, 637.
22 M. Zoghi, M. Pourmadadi, F. Yazdian, M. N. Nigjeh, H. Rashedi and R. Sahraeian, Synthesis and characterization of chitosan/carbon quantum dots/Fe2O3 nanocomposite comprising curcumin for targeted drug delivery in breast cancer therapy, *Int. J. Biol. Macromol.*, 2023, **249**, 125788.
23 Y. Yan, Y. Sun, Y. Li, Z. Wang, L. Xue and F. Wang, Advancing cancer therapy: Nanomaterial-based encapsulation strategies for enhanced delivery and efficacy of curcumin, *Mater. Today Bio*, 2025, **33**, 101963.
24 E. M. Alshammari, Curcumin-based biocompatible nanocarriers: a contemporary perspective in functional foods and biomedical applications, *Discover Nano*, 2025, **20**, 226.
25 R. Maurya, S. Ramteke and N. K. Jain, Quality by design (QbD) approach-based development of optimized nanocarrier to achieve quality target product profile (QTPP)-targeted lymphatic delivery, *Nanotechnology*, 2024, **35**, 265101.
26 J. G. Duarte, M. G. Duarte, A. P. Piedade and F. Mascarenhas-Melo, Rethinking pharmaceutical industry with quality by design: application in research, development, manufacturing, and quality assurance, *AAPS J.*, 2025, **27**, 96.
27 L. X. Yu, G. Amidon, M. A. Khan, S. W. Hoag, J. Polli, G. K. Raju and J. Woodcock, Understanding pharmaceutical quality by design, *AAPS J.*, 2014, **16**, 771–783.
28 A. K. Sah and P. K. Suresh, Loteprednol etabonate nanoparticles: optimization via Box-Behnken design response surface methodology and physicochemical characterization, *Curr. Drug Delivery*, 2017, **14**, 676–689.
29 S. L. C. Ferreira, R. E. Bruns, H. S. Ferreira, G. D. Matos, J. M. David, G. C. Brandão, E. G. P. da Silva, L. A. Portugal, P. S. Dos Reis and A. S. Souza, Box-Behnken design: An alternative for the optimization of analytical methods, *Anal. Chim. Acta*, 2007, **597**, 179–186.
30 P. Majewski and B. Thierry, Functionalized magnetite nanoparticles—synthesis, properties, and bio-applications, *Crit. Rev. Solid State Mater. Sci.*, 2007, **32**, 203–215.
31 K. I. Priyadarsini, The chemistry of curcumin: from extraction to therapeutic agent, *Molecules*, 2014, **19**, 20091–20112.
32 M. Kharat, Z. Du, G. Zhang and D. J. McClements, Physical and chemical stability of curcumin in aqueous solutions and emulsions: impact of pH, temperature, and molecular environment, *J. Agric. Food Chem.*, 2017, **65**, 1525–1532.
33 H. Zheng, Y. Zhang, L. Liu, W. Wan, P. Guo, A. M. Nystrom and X. Zou, One-pot synthesis of metal–organic frameworks with encapsulated target molecules and their applications for controlled drug delivery, *J. Am. Chem. Soc.*, 2016, **138**, 962–968.
34 A. Mittal, S. Gandhi and I. Roy, Mechanistic interaction studies of synthesized ZIF-8 nanoparticles with bovine serum albumin using spectroscopic and molecular docking approaches, *Sci. Rep.*, 2022, **12**, 10331.
35 R. E. Des Bouillons-Gamboa, G. Montes de Oca, J. R. V. Baudrit, L. C. Ríos Duarte, M. Lopretti, M. Rentería Urquiza, J. M. Zúñiga-Umaña, F. Barreiro and P. Vázquez, Synthesis of chitosan nanoparticles (CSNP): effect of CH-CH-TPP ratio on size and stability of NPs, *Front. Chem.*, 2024, **12**, 1469271.
36 C. Mircioiu, V. Voicu, V. Anuta, A. Tudose, C. Celia, D. Paolino, M. Fresta, R. Sandulovici and I. Mircioiu, Mathematical modeling of release kinetics from supramolecular drug delivery systems, *Pharmaceutics*, 2019, **11**, 140.
37 Y. Zhang, M. Huo, J. Zhou, A. Zou, W. Li, C. Yao and S. Xie, DDSolver: an add-in program for modeling and comparison of drug dissolution profiles, *AAPS J.*, 2010, **12**, 263–271.

38 E. K. Droepenu, E. Amenyogbe, M. A. Boatemaa and E. Opoku, Study of the antimicrobial activity of zinc oxide nanostructures mediated by two morphological structures of leaf extracts of Eucalyptus robusta Sm, *Heliyon*, 2024, **10**(4), e25590.

39 T. Mosmann, Rapid colorimetric assay for cellular growth and survival: application to proliferation and cytotoxicity assays, *J. Immunol. Methods*, 1983, **65**, 55–63.

40 I. C. for Harmonisation, *ICH Q1A (R2): Stability testing of new drug substances and products*, International Council for Harmonisation, 2003, vol. 1, pp. 1–24.

41 R. Ettlinger, N. Moreno, N. Ziółkowska, A. Ullrich, H. Krug von Nidda, D. Jirák, K. Kerl and H. Bunzen, In vitro studies of Fe3O4-ZIF-8 core–shell nanoparticles designed as potential theragnostics, *Part. Part. Syst. Char.*, 2020, **37**, 2000185.

42 J. Kong, S. Xu, Y. Dai, Y. Wang, Y. Zhao and P. Zhang, Study of the Fe3O4@ ZIF-8@ sor composite modified by tannic acid for the treatment of sorafenib-resistant hepatocellular carcinoma, *ACS Omega*, 2023, **8**, 39174–39185.

43 S. K. Filippov, R. Khusnutdinov, A. Murmiliuk, W. Inam, L. Y. Zakharova, H. Zhang and V. V Khutoryanskiy, Dynamic light scattering and transmission electron microscopy in drug delivery: a roadmap for correct characterization of nanoparticles and interpretation of results, *Mater. Horiz.*, 2023, **10**, 5354–5370.

44 B. K. Wilson and R. K. Prud'homme, Nanoparticle size distribution quantification from transmission electron microscopy (TEM) of ruthenium tetroxide stained polymeric nanoparticles, *J. Colloid Interface Sci.*, 2021, **604**, 208–220.

45 Wahajuddin and S. Arora, Superparamagnetic iron oxide nanoparticles: magnetic nanoplatforms as drug carriers, *Int. J. Nanomed.*, 2012, 3445–3471.

46 H. M. Fahmy, S. Shekewy, F. A. Elhusseiny and A. Elmekawy, Enhanced biocompatibility by evaluating the cytotoxic and genotoxic effects of magnetic iron oxide nanoparticles and chitosan on Hepatocellular Carcinoma Cells (HCC), *Cell Biochem. Biophys.*, 2024, **82**, 1027–1042.

47 A. Criveanu, F. Dumitrache, C. Fleaca, L. Gavrila-Florescu, I. Lungu, I. P. Morjan, V. Socoliuc and G. Prodan, Chitosan-coated iron oxide nanoparticles obtained by laser pyrolysis, *Appl. Surf. Sci. Adv.*, 2023, **15**, 100405.

48 F. Parsa, M. Setoodehkhah and S. M. Atyabi, Design, fabrication and characterization of a magnetite-chitosan coated iron-based metal–organic framework (Fe 3 O 4@ chitosan/MIL-100 (Fe)) for efficient curcumin delivery as a magnetic nanocarrier, *RSC Adv.*, 2025, **15**, 18518–18534.

49 S. Hansapaiboon, B. P. Bulatao, F. N. Sorasitthiyanukarn, P. Jantaratana, N. Nalinratana, O. Vajragupta, P. Rojsitthisak and P. Rojsitthisak, Fabrication of Curcumin Diethyl γ-Aminobutyrate-Loaded Chitosan-Coated Magnetic Nanocarriers for Improvement of Cytotoxicity against Breast Cancer Cells, *Polymers*, 2022, **14**, 5563.

50 A. M. El-Khawaga, M. Ayman, O. Hafez and R. E. Shalaby, Photocatalytic, antimicrobial and antibiofilm activities of MgFe2O4 magnetic nanoparticles, *Sci. Rep.*, 2024, **14**, 12877.

51 Y. Rahvar, N. Motakef-Kazemi and R. Hosseini Doust, Synthesis of Zn2 (BDC) 2 (DABCO) MOF by solution and solvothermal methods and evaluation of its anti-bacterial, *Nanomed. Res. J.*, 2021, **6**, 360–368.

52 M. Górski, J. Niedźwiadek and A. Magryś, Antibacterial activity of curcumin–a natural phenylpropanoid dimer from the rhizomes of Curcuma longa L. and its synergy with antibiotics, *Ann. Agric. Environ. Med.*, 2022, **29**, 394–400.

53 A. Sirelkhatim, S. Mahmud, A. Seeni, N. H. M. Kaus, L. C. Ann, S. K. M. Bakhori, H. Hasan and D. Mohamad, Review on zinc oxide nanoparticles: antibacterial activity and toxicity mechanism, *Nano-Micro Lett.*, 2015, **7**, 219–242.

54 P. Nisar, N. Ali, L. Rahman, M. Ali and Z. K. Shinwari, Antimicrobial activities of biologically synthesized metal nanoparticles: an insight into the mechanism of action, *JBIC, J. Biol. Inorg. Chem.*, 2019, **24**, 929–941.

55 M. I. Anik, M. K. Hossain, I. Hossain, A. Mahfuz, M. T. Rahman and I. Ahmed, Recent progress of magnetic nanoparticles in biomedical applications: A review, *Nano Sel.*, 2021, **2**, 1146–1186.

56 Q. Abbas, M. Zia-ur-Rehman, H. Ullah, M. A. M. Munir, M. U. Ali, A. Ali, K. Pikon and B. Yousaf, Recent advances in the detection and quantification of manufactured nanoparticles (MNPs) in complex environmental and biological matrices, *J. Cleaner Prod.*, 2024, **471**, 143454.

57 S. Naz, S. Jabeen, S. Ilyas, F. Manzoor, F. Aslam and A. Ali, Antibacterial activity of Curcuma longa varieties against different strains of bacteria, *Pak. J. Bot.*, 2010, **42**, 455–462.

58 N. M. Wada, A. A. Ambi, A. A. Ibrahim, S. K. Bello, A. Umar and D. T. James, Antimicrobial Activity of Extracts of Turmeric (Curcuma longa) and Garlic (Aliium sativum) Against Selected Bacterial Clinical Isolates, *Mediterr. J. Infect. Microbes Antimicrob.*, 2021, **10**(1), 6.

59 C. Tamames-Tabar, D. Cunha, E. Imbuluzqueta, F. Ragon, C. Serre, M. J. Blanco-Prieto and P. Horcajada, Cytotoxicity of nanoscaled metal–organic frameworks, *J. Mater. Chem. B*, 2014, **2**, 262–271.

60 M. Xu, Y. Hu, W. Ding, F. Li, J. Lin, M. Wu, J. Wu, L.-P. Wen, B. Qiu and P.-F. Wei, Rationally designed rapamycin-encapsulated ZIF-8 nanosystem for overcoming chemotherapy resistance, *Biomaterials*, 2020, **258**, 120308.

61 C.-Y. Sun, C. Qin, X.-L. Wang, G.-S. Yang, K.-Z. Shao, Y.-Q. Lan, Z.-M. Su, P. Huang, C.-G. Wang and E.-B. Wang, Zeolitic imidazolate framework-8 as efficient pH-sensitive drug delivery vehicle, *Dalton Trans.*, 2012, **41**, 6906–6909.

62 K. Maruyama, Intracellular targeting delivery of liposomal drugs to solid tumors based on EPR effects, *Adv. Drug Delivery Rev.*, 2011, **63**, 161–169.

63 Y. Liu, D. Liu, L. Zhu, Q. Gan and X. Le, Temperature-dependent structure stability and in vitro release of chitosan-coated curcumin liposome, *Food Res. Int.*, 2015, **74**, 97–105.

64 B. Zheng, X. Zhang, H. Lin and D. J. McClements, Loading natural emulsions with nutraceuticals using the pH-driven

method: formation & stability of curcumin-loaded soybean oil bodies, *Food Funct.*, 2019, **10**, 5473–5484.

65 C. Winarti and T. C. Sunarti, Effect of Heating on the Stability of Curcumin on Temulawak Oleoresin Encapsulated in Arrowroot Starch Nanoparticles, in *E3S Web of Conferences*, EDP Sciences, 2022, p. 4005.

66 C. Freitas and R. H. Müller, Effect of light and temperature on zeta potential and physical stability in solid lipid nanoparticle (SLN™) dispersions, *Int. J. Pharm.*, 1998, **168**, 221–229.

67 H. H. S. Food and Drug Administration, *International Conference on Harmonisation; guidance on Q6A specifications: test procedures and acceptance criteria for new drug substances and new drug products: chemical substances*, Federal Register, 2000, vol. 65, pp. 83041–83063.

68 I. H. T. Guideline, *Stability testing of new drug substances and products, Q1A (R2), Current Step 4*, 2003.